Università degli Studi di Milano-Bicocca

School of Mathematics, Physics and Natural Sciences

Master's Degree Course in Physics

Master's Degree Thesis

Study of Spatial and Angular Resolution of SPACAL Prototypes for the LHCb ECAL Upgrade II.

Supervisors:
Dott. Marco Pizzichemi
Prof. Marta Calvi

Candidate:
Giorgia Bonomelli

ACADEMIC YEAR 2021–2022

This page intentionally left blank.

RIASSUNTO

Il Large Hadron Collider (LHC) del CERN è l'acceleratore di particelle più grande e potente del mondo e rappresenta la chiave per comprendere la nuova frontiera della fisica delle alte energie. Per sostenere e incrementare il suo potenziale di scoperta, nel corso dei prossimi anni verrà eseguito un importante upgrade per raggiungere una luminosità massima di $5 \times 10^{34} cm^{-2} s^{-1}$. La nuova configurazione, nota come High Luminosity LHC (HL-LHC), fornirà misure più accurate di nuove particelle e consentirà di osservare processi rari che si verificano al di sotto dell'attuale soglia di sensibilità.
Tuttavia, durante questa fase i livelli di radiazione saranno molto più alti dei valori nominali per i quali sono stati progettati gli esperimenti di LHC. Tra questi, LHCb (Large Hadron Collider beauty) rappresenta un esperimento dedicato alla fisica del sapore, progettato per lo studio di particelle contenenti quark b o c, della violazione di CP e dei decadimenti rari per cercare prove indirette di nuova fisica. Il rivelatore, che è uno spettrometro a braccio singolo con copertura angolare in avanti, ha una geometria particolare per rilevare coppie di adroni $b\bar{b}$ che sono prodotte a piccoli angoli nelle collisioni protone-protone.
Per la fase HL-LHC, i componenti dello spettrometro dovranno essere modificati e possibilmente potenziati per raggiungere prestazioni migliori e allo stesso tempo operare in un ambiente che prevede radiazioni più elevate con dosi fino a 1 MGy. In particolare, dovrà essere introdotto un cambiamento importante anche nella progettazione del calorimetro elettromagnetico e nella scelta dei materiali per il suo upgrade. L'obiettivo dell'Upgrade II di ECAL è quello di dotare l'intero calorimetro di una granularità più elevata (circa 2 cm) e di informazioni temporali più precise, dell'ordine di alcune decine di picosecondi per ridurre il pile-up, mantenendo la risoluzione energetica almeno pari a quella attuale.
Attualmente, una possibile soluzione è lo Spaghetti Calorimeter (SpaCal), un calorimetro sampling costituito da un assorbitore denso in cui sono inserite fibre scintillanti. I materiali promettenti per lo SpaCal sono il tungsteno (W) e il piombo (Pb) per l'assorbitore, puri o in lega, e il granato drogato di cerio (YAG, GAGG) o le fibre di polistirene per la parte attiva del modulo.
Il piano attuale per l'Upgrade II di ECAL prevede l'inserimento di due regioni interne aggiuntive per aumentare la granularità e affrontare i problemi causati dalla sovrapposizione dei cluster, ovvero una regione di 1,5x1,5cm^2 e una di 3x3cm^2. Data la necessità di materiali altamente resistenti alle radiazioni, si è deciso di utilizzare fibre di cristalli nella regione centrale come parte attiva del rivelatore. Per la regione più interna è stato costruito un primo prototipo con un assorbitore al W, dotato di fibre di YAG e GAGG, mentre per l'altra regione è stato allestito un altro modulo con un assorbitore di piombo e fibre di polistirene.

Questa tesi presenta l'analisi dell'insieme di dati acquisiti in vari test su fascio presso il Super Proton Synchrotron (SPS) del CERN con elettroni-positroni nell'intervallo di energia 20-100 GeV, e presso la facility di DESY tra 1-5,8 GeV, dove queste tecnologie innovative sono state studiate e hanno ottenuto risultati promettenti, raggiungendo un termine sampling e costante per la risoluzione energetica di circa 10 e 1% e una risoluzione temporale di 10-20 ps.
In particolare, questo progetto di ricerca si concentra principalmente sulla risoluzione spaziale e angolare dei nuovi prototipi SpaCal, in quanto per separare in modo efficace le shower elettromagnetiche che si sovrappongono sono necessarie una conoscenza precisa dell'angolo della traiettoria e una risoluzione sulla posizione della particella dell'ordine di 1 mm. Inoltre, queste informazioni sono essenziali anche per una ricostruzione precisa della posizione delle particelle cariche e neutre per il prossimo upgrade. A questo scopo, sono stati testati diversi angoli di rotazione dei moduli e la risoluzione spaziale è stata studiata principalmente variando l'energia

del fascio e in funzione della posizione all'interno della cella centrale del prototipo in esame. Inoltre, i risultati ottenuti nei test su fascio relativi ai due moduli SpaCal che saranno installati durante l'Upgrade II del rivelatore LHCb sono stati confrontati con le simulazioni Monte Carlo, in cui è stato riprodotto in modo dettagliato il setup utilizzato durante l'acquisizione dei dati.

I valori sperimentali di risoluzione spaziale e angolare raggiunti, confermati anche dai risultati delle simulazioni MC, hanno dimostrato il potenziale delle fibre GAGG, non solo in termini di resistenza alle radiazioni ma anche per la loro ottimale risoluzione sulla posizione delle particelle, confermando le proprietà promettenti di questi cristalli che saranno implementati nella parte più interna del rivelatore. D'altra parte, le prestazioni del prototipo SpaCal Pb in termini di risoluzione spaziale e angolare sono leggermente peggiori rispetto allo SpaCal W, raggiungendo valori sotto a 1 mm e $>1°$ rispettivamente.
Tuttavia, entrambi i moduli SpaCal soddisfano i requisiti per l'Upgrade previsto per la fase II di LHC, mantenendo una risoluzione energetica pari a quella attuale, una risoluzione sulla posizione che garantisce la separazione delle shower che si sovrappongono e delle performance temporali che consentono una ricostruzione accurata degli eventi associati ai π_0 e una riduzione del fondo combinatorio relativo ai γ.

ABSTRACT

The Large Hadron Collider (LHC) at CERN is the world's largest and most powerful particle accelerator and it represents the key to understand the new frontier of high-energy physics. To sustain and increase its discovery potential, a major upgrade will take place during the 2020s to achieve a peak luminosity of $5 \times 10^{34} cm^{-2} s^{-1}$. The new configuration, known as High Luminosity LHC (HL-LHC), will provide more accurate measurements of new particles and enable the observation of rare processes that occur below the current sensitivity threshold.

However, during this phase the radiation levels will be much higher than the nominal values for which the LHC experiments were designed. Among these, LHCb (Large Hadron Collider beauty) represents an experiment dedicated to heavy flavour physics, designed for the study of particles containing b or c quarks, CP violation and rare decays to look for indirect evidence of new physics. The detector, which is a single-arm forward spectrometer with a forward angular coverage, has a peculiar geometry to detect $b\bar{b}$ hadron pairs that are produced at small polar angles in proton-proton collisions.

For the HL-LHC Phase, the spectrometer components will need to be modified, and possibly improved to achieve better performance while operating in a higher radiation environment with doses up to 1 MGy. In particular, a major change will also have to be introduced in the design of the electromagnetic calorimeter and in the choice of materials for its upgrade. The aim of the ECAL Upgrade II is to provide the whole detector with higher granularity (around 2 cm) and precise timing information, of the order of a few tens of picoseconds to reduce pileup, while keeping the energy resolution at least as the current one.

Presently, a solution being investigated is the Spaghetti Calorimeter (SpaCal), which is a sampling calorimeter made of a dense absorber in which scintillating fibres are inserted. The promising materials for the SpaCal are Tungsten (W) and Lead (Pb) for the absorber, either pure or alloys, and Cerium-doped Garnet (YAG, GAGG) or Polystyrene fibres for the active part of the module.

The current plan for the ECAL Upgrade II is to insert two additional inner regions to increase the granularity and to deal with the problems caused by overlapping clusters, namely a 1.5x1.5cm^2 and a 3x3cm^2 region. Given the necessity of highly radiation hard materials, it was decided to employ crystal fibres in the central region as the active part of the detector. For the innermost area a first prototype was built out of a Tungsten absorber, equipped with Garnet crystal fibres (YAG, GAGG), while for the other region another module with a Lead absorber and Polystyrene fibres has been set up.

This thesis presents the analyses of the datasets acquired in various beam tests at the Super Proton Synchrotron (SPS) at CERN with an electron-positron beam in the energy range of 20-100 GeV, and at DESY facility between 1-5.8 GeV, where these innovative technologies were investigated and achieved promising results, reaching an energy resolution sampling and constant terms of about 10 and 1% and a time resolution of a 10-20 ps.

In particular, this research project is mainly focused on the spatial and angular resolution of the new SpaCal prototypes, since a precise knowledge of the angle of the trajectory and a resolution on the position of the particle of the order of 1 mm are required to separate in an effective way the overlapping showers. In addition, these information are essential also for a precise reconstruction of the position for both the charged and neutral particles for the next upgrade. For this purpose, several rotation angles of the modules were tested, and the spatial resolution was investigated mainly varying the beam energy as well as a function of the position within the central cell of the prototype under examination.

Furthermore, the results of the two SpaCal modules that will be installed during the Upgrade II of the LHCb detector obtained from the beam tests were compared with the outcome of detailed Monte Carlo simulations, where the test-beam setup used for the data acquisition was reproduced.

The values achieved for the spatial and the angular resolution in the Beam Tests, that have also been confirmed by MC simulation results, demonstrated the potential of the GAGG fibres, not only in terms of radiation hardness but also for their position and angular ability confirming the promising properties of these crystals that will be employed for the innermost part of the detector. On the other hand, the performances of the SpaCal Pb prototype in terms of spatial and angular resolution are slightly worse than the SpaCal W, reaching values below 1 mm and $>1^\circ$ respectively.

Nevertheless, both SpaCal modules meet the requirements for the Upgrade forseen for the LHC Phase II, by keeping the energy resolution as the current one, a position resolution that guarantees the separation of the overlapping showers, and a time performance that allows an accurate reconstruction of π_0 events as well as a reduction of the γ combinatorial background.

Aim of the Thesis

The aim of this thesis is to investigate the performances of the SpaCal prototypes in terms of the angular and spatial resolution, which are strictly correlated to each other.
A position ability around 1 mm for the ECAL would guarantee first an efficient separation of the overlapping showers, and secondly a precise reconstruction of the position for both neutral and charged particles. For the charged ones, the signals in ECAL are matched with the trajectories reconstructed from the tracking detector to perform an accurate particle identification. As for the neutral particles, the position measurement is only available from the calorimeter, and it is fundamental to reconstruct events.
Also a good angular resolution is required for the Upgrade II of the ECAL to study theories with physics beyond the Standard Model that involve particles with a detectable decay length from the interaction point, known as Long-Lived Particles (LLP).

To investigate their performance, the modules were tested both at SPS and at DESY facilities, and the results were compared with the outcome of detailed Monte Carlo simulations, where the test-beam setup used for the data acquisition was reproduced.

Contents

Chapter 1

Theoretical Background

This chapter deals with some theoretical aspects required for the understanding of this thesis, starting from the interaction of the radiation with matter that enters in every detector performance description, to the introduction to calorimetry and the detailed description of electromagnetic shower development within the detector.

1.1 Radiation Interaction

The operation of any radiation detector depends on the way the radiation interacts with the material of the detector itself. Therefore to understand the response of a detector it is essential to know the mechanism by which radiations interact and lose their energy in matter.

1.1.1 Interaction of Electrons

The energy loss of light charged particles such as electrons or positrons causes the ionisation or the excitation of the medium, which is described by an expression derived by the Bethe formula, called *collisional loss.*

$$-\left(\frac{dE}{dx}\right)_c = \frac{2\pi e^4 NZ}{m_0 v^2}\left(ln\frac{m_0 v^2 E}{2I^2(1-\beta^2)} - (2\sqrt{1-\beta^2}-1+\beta^2)ln2+1-\beta^2+\frac{1}{8}(1-\sqrt{1-\beta^2})^2\right) \tag{1.1}$$

The energy loss through collision is expressed in Equation 1.1, where $\beta = v/c$ is a function of the velocity v of the electron, N and Z are the number density and the atomic number of the absorber atoms, m_0 the electron rest mass and e its charge. The parameter I represents the average excitation and ionisation potential of the absorber medium.
Since the electron mass is equal to that of the orbital electrons with which they interact, large deviations in electron path are observed, and a large fraction of their energy can be lost in a single step.
Electrons may also lose energy through radiative processes, which take the form of *bremsstrahlung* or electromagnetic radiation usually emitted along the electron track.

From classical theory the radiative emission results from the acceleration of a charged particle, which in this case is reflected by the deflection of the electron due to its interaction with the absorber.

$$-\left(\frac{dE}{dx}\right)_r = \frac{NEZ(Z+1)e^4}{137m_0^2c^4}\left(4ln\frac{2E}{m_0c^2} - \frac{4}{3}\right) \tag{1.2}$$

This phenomenon is described by Equation 1.2, where the symbols have the same meaning as Equation 1.1.

Then the total stopping power for the electron is the sum of the radiative and collisional losses. The ratio of the specific energy losses is approximately

$$\frac{(dE/dx)_r}{(dE/dx)_c} \simeq \frac{EZ}{700} \tag{1.3}$$

where E is in units of MeV. From the expression 1.3, one can conclude that for energies around 1MeV the radiative losses are a small fraction of the total energy loss.

1.1.2 Interaction of Photons

Three major types of interactions between gammas and matter take place: photoelectric absorption, Compton scattering and pair production.

In the **Photoelectric absorption** process the photon is completely absorbed by the atom with which it is interacting. Then an energetic photoelectron is ejected by the atom from one of its bound shells, with an energy given by

$$E_e = h\nu - E_b \tag{1.4}$$

where E_b represents the binding energy of the electron in its original shell and $h\nu$ the energy of the incoming photon. It is more probable for this effect to occur on the K shell of the atom if the photon has a sufficient energy.

The photoelectric process is the predominant mode of interaction for gamma rays of low energies, and it is enhanced for absorber materials of high atomic number Z ($\sim Z^n$ with $4 < n < 5$).

The **Compton scattering** takes place between the photon and an external electron of the absorbing material. The gamma transfers a fraction of his energy to the electron, resulting then with a lower energy $h\nu'$ at the end of the process, and it is deflected through an angle θ with respect to the original direction. The portion of energy transferred can vary from zero to a large fraction of the photon initial energy, and it depends on the scattering angle according to the following expression:

$$h\nu' = \frac{h\nu}{1 + \frac{h\nu}{m_0c^2}(1 - cos\theta)} \tag{1.5}$$

The probability of Compton scattering depends on the number of electrons available as scattering targets, therefore it increases linearly with Z.

The **Pair Production** is a threshold process that occurs only when the photon energy

exceeds twice the rest-mass energy of an electron. However the probability of this interaction is low until the photon energy reaches several MeV. This effect fully replaces the gamma ray, which disappears, with an electron-positron pair. The new particles carry the photon's excess energy as kinetic energy. The positron annihilates immidiately after its production, then two annihilation photons will be generated as secondary products of the interaction.
The probability of pair production rises sharply with energy and approximately as the square of the absorber atomic number ($\sim Z^2$).

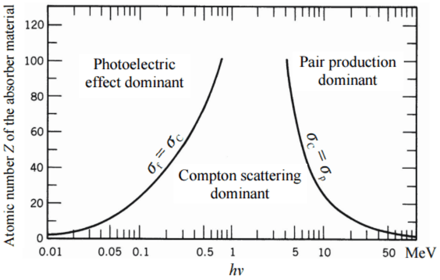

Figure 1.1: Importance of the three major types of gamma ray interactions. The lines show the the values of Z and $h\nu$ for which the two neighboring effects are equal (Picture from [7]).

The Figure 1.1 describes the importance of the three main processes for the gammas as a function of their initial energy and for different absorbing materials. It is possible then to notice that the plot is divided into three regions: each of them is dominated by either photoelectric absorption, Compton scattering or pair production.

1.2 Calorimetry

Calorimetry comprises all the experimental methods that aim to measure the energy of particles. In nuclear and particle physics for instance, the calorimeter is a block of matter which measures the total energy lost by a particle through a destructive process, and produces a signal proportional to the particle energy.
In modern particle physics experiments, calorimeters fulfill different tasks, each with its own specific requirements in terms of detector performance. A properly designed calorimeter system has all these requirements taken into account.
The choices of the technology and of the detector parameters for a specific application usually are related to the physics processes one wants to study, the available budget, the radiation levels and other operating conditions in the environment where the experiment takes place. Building a calorimetry system involves not only the choice of the materials, but also the geometrical design, that includes the longitudinal and the lateral segmentation of the detector, and the electronic readout of the various segments. This should be a compromise to optimise the detector performance in all areas of interest.

The choice of a certain calorimeter system is often supported by the results from prototype tests in particle beams. However, one must be careful since the material affects every particle in a different way. Therefore the results of tests with electron beams cannot be assumed to be also valid for other particles and viceversa. Another important reason for caution in the interpretation of test beam results concerns the fact that the experimental conditions are fundamentally different from those in the experiment in which the calorimeter is involved. For instance during a test beam, particles of a known type and a precisely known energy are used, while in the experiment there is a large range of energies and different particles involved.

In a calorimetry system, the absorption of a particle can generate signals of different nature, depending on the material. In most cases, in collider experiments the signal depends on the energy deposited by the shower particles in the sensitive part of the detector. There may be a light output if the calorimeter is made of scintillators, or ionisation charge signal if there is gaseous or semiconductive active material. In addition, calorimeters may be able to measure also the position of the particle and other properties based on its design and segmentation.

A generic classification exists for calorimeters, which can be divided into two main categories: *homogeneous* and *sampling* calorimeters. The former describes a category of detectors whose entire volume is sensitive to the particles, then all the energy deposited is converted into signal. Indeed the function of absorbing the particles and detecting the signals resulting from this process are exercised by the same medium. This should be an high-density material in order to perform the first function efficiently.
On the other hand, the latter represents the devices in which the functions of particle absorption and signal generation are exercised by different materials, called respectively the passive and active medium. The first one is typically a high-density material, and the second one generates the light or charge that forms the basis for the signals from this calorimeter. Then in this case only a fraction of the deposited energy is converted into signal (i.e. the energy deposited in the sensitive material).

Calorimeters are instruments built to measure energy. The precision with which this is done is the most important parameter for this type of detectors, and is known as *energy resolution*. This quantity is typically determined as the relative width of a signal distribution given by a particle of precisely known energy, extrapolated from a Gaussian fit of the data.
For the sampling calorimeters the energy resolution is usually limited by instrumental effects, such as fluctuations in the light collection efficiency of the crystals. In general, the shower electrons that deposit energy into the absorber material do not contribute to the calorimeter signal at all and sampling fluctuations may be interpreted as the statistical fluctuations in the number of different shower electrons that do contribute. This number can be increased by incorporating more active layers of a given type, or by reducing the

thickness of the individual active elements for a given total amount of active material.

$$\frac{\sigma}{E} = \frac{noise}{E} \oplus \frac{sampling}{\sqrt{E}} \oplus const \tag{1.6}$$

The general expression for the energy resolution is described by Equation 1.6, where the sampling term includes the shower intrinsic fluctuations due to alternating layers of absorber and active medium, the noise term comes from the electronic noise of the readout chain, and the constant contribution derives from instrumental effects that cause variations of the calorimeter response with the particle impact point on the detector.

1.3 Electromagnetic Shower Development

An electromagnetic shower is a cascade process consisting of a large production of secondary particle that results from the energy loss due to the interaction of electromagnetic particles with matter. Already at energies above 1GeV and in many materials the principal source of energy loss is the bremsstrahlung for electrons and positrons, and the pair production for photons.
As mentioned in the section 1.1, the bremsstrahlung is a radiative process that produces photons. These in turn, interact with matter through photoelectric absorption or Compton scattering, and only if their energy is high enough, through pair production.
On the other hand the primary photons that perform pair production, generate an electron-positron pair, where the positron annihilates into photons and the electron loses energy in the material through ionisation or radiative processes.
Then the secondary particles produced by the primaries interact through the same processes leading to the development of a particle shower inside the calorimeter. The shower development stops when the electrons are slowed down to energy values such that the energy loss from ionisation is more probable than from bremsstrahlung.

It is useful to define the *critical energy* E_c in the electromagnetic shower description as the value of energy at which the loss rates from ionisation and from bremsstrahlung become equal. There is an empirical description of this quantity which is derived from experimental measurements:

$$E_c = \frac{610}{Z + 1.24} MeV \quad \text{for liquids and solids} \tag{1.7}$$

$$E_c = \frac{710}{Z + 0.92} MeV \quad \text{for gases} \tag{1.8}$$

This represents a crucial parameter in the choice of the calorimeter material, and it is also strongly related to the shower development inside the calorimeter. Indeed the *shower maximum* is reached when the average energy of the shower particles equals the critical energy. As the shower develops, the average energy of the shower particles decreases, and the shower maximum represents the depth at which no further multiplication takes place. Beyond this point, the shower photons are more likely to produce one electron with Compton or photoelectric interactions, rather than an electron–positron pair. And in turn the electrons and positrons lose their energy mainly through ionization of the absorber medium, rather than through radiation. Therefore, beyond the shower maximum the number of shower particles, and thus the energy deposited in a detector layer gradually decreases.

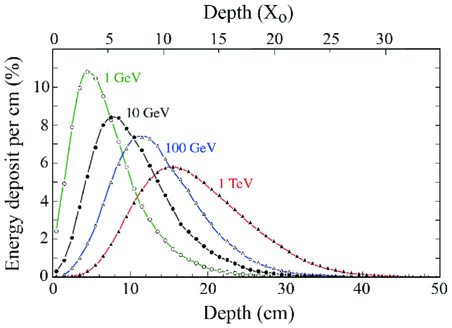

Figure 1.2: The percentage of energy deposit as a function of depth in a block of copper, for 1, 10, 100 and 1,000 GeV electron showers . The integrals are normalized to the same value(Picture from [8]).

For instance, the Figure 1.2 shows the energy deposit as a function of depth, for 1, 10, 100 and 1,000 GeV electron showers developing in a block of copper. The higher the initial energy of the showering particle, the longer the particle multiplication phase continues.

There are other parameters that are frequently used to describe the characteristic shower dimensions: the *radiation length* X_0 for the longitudinal development and the *Molière radius* R_M for the lateral development.

Radiation Length The radiation length is defined as the mean distance over which an electron or positron loses on average, 63.2% (i.e. (1 - 1/e)) of its energy to bremsstrahlung. Approximately it can be parametrised as

$$X_0 = \frac{716.4\, A}{Z(Z+1)\, ln(187/\sqrt{Z})}\; g/cm^2 \tag{1.9}$$

From the Equation 1.9 the dependence of the radiation length from the material is evident. Moreover $X_0 = 180 \cdot A/Z^2\, (g/cm^2)$ is a further approximation of the Equation 1.9 that express the relation between the radiation length and the mass and the atomic number of the absorber.

Since the mean distance traveled by a photon before it is converted to an e^+e^- pair with probability (1 - 1/e) is $\frac{9}{7}X_0$, the shower produced by the photon will start slightly later with respect to electrons.

Molière Radius The Molière radius is frequently used to describe the transverse development of the electromagnetic showers in terms of the radiation length X_0 and the critical energy E_c.

$$R_M = E_s \frac{X_0}{E_c} \tag{1.10}$$

where E_s is the energy scale defined as $m_e c^2 \sqrt{4\pi/\alpha} = 21.2$ MeV.
In addition, R_M represents the radius around the shower axis of a cylinder of infinite length that contains $\sim 85-90\%$ of the energy deposited by the shower.

The Molière radius is less Z dependent than the radiation length, which decreases when Z grows as $\sim 1/Z$ if we assume A is proportional to Z. Since the critical energy also scales approximately in the same way, from Equation 1.10 it results that the Z dependence cancels in first approximation.
As a consequence of this difference in Z dependence, the development of the electromagnetic shower has very different characteristics if two different materials are used.

Shower Profiles Since the radiation length and the Molière radius were defined to eliminate the material-dependent effects, the development of the electromagnetic shower, expressed in X_0 and R_M units, is approximately Z independent.

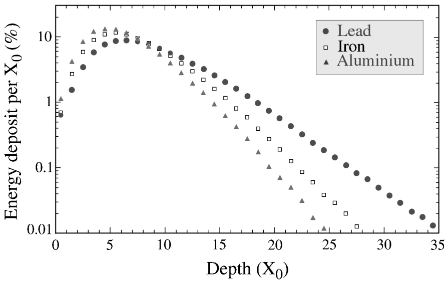

Figure 1.3: Longitudinal development of 10 GeV electron showers in Al, Fe and Pb as a function of depth (Picture from [8]).

Indeed, from the Figure 1.3 the profiles appear to be very similar due to the scaling with the radiation length. However, some differences can be noticed depending on the absorber material considered: as Z increases the shower maximum is shifted to a greater depth and after that the profiles decay more slowly. Therefore, the higher the material density, the larger the number of X_0 needed to contain the electromagnetic shower.
It is fundamental for the purpose of this thesis to introduce the *Centre Of Gravity (COG)* of the electromagnetic shower, which is defined as the 3D barycenter of the cluster (x_c, y_c, z_c). Since there is a logarithmic energy dependence of the depth at which the shower maximum occurs, it is possible to introduce a parametrisation which describes this relation.

$$z_c = p_0 + p_1\, ln(E) \tag{1.11}$$

The Equation 1.11, called **L-correction**, represents the position of the longitudinal barycenter of the shower z_c corrected from the penetration depth of the particle [9].

The electromagnetic shower profiles have also a spread in the plane perpendicular to the direction of the incoming particle, which is caused by different effects. The process that dominates in early stages of the shower development involves mainly electrons and positrons, that move away from the propagation axis because of multiple Coulomb scattering. Instead beyond the shower maximum photons that interacts through more isotropic processes as Compton scattering and Photoelectric effect are involved.
Assuming the transversal shower shape to be exponential $E(r) \sim E_0 e^{-\frac{r}{b}}$, the transversal barycenter (x_c, y_c) is evaluated from the energy-weighted barycenter of the cluster (x_b, y_b) corrected from the non linear transversal profile of the shower.

$$(x_c, y_c) = b \cdot asinh\left[\frac{(x_b, y_b)}{\Delta}\, cosh\frac{\Delta}{b}\right] \tag{1.12}$$

The Equation 1.12 represents the **S-correction** that returns the corrected centre-of-gravity coordinates. In this expression b is the decay constant of the exponential profile, and Δ is half the cellsize.

During the design phase of a calorimeter system for a specific experiment, it is important for the detector to be sufficiently large to contain the electromangetic shower on avarage at a certain level, e.g. 95%. Shower particles escaping from the detector represent a source of fluctuations that may affect the precision of the measurements. The effects of the shower leakages on the energy resolution and other aspects of the calorimeter are determined event by event. In particular, it turns out that the performance of the detector are affected more by the longitudinal shower leakage than by transverse shower leakage at the same percentage level.

Chapter 2

LHCb detector at Large Hadron Collider

The Large Hadron Collider beauty (LHCb) [1] experiment is one of the four main particle detectors located at one of the four collision points around the ring of the Large Hadron Collider (LHC) at CERN.
After a brief introduction on the LHC, this chapter will give an overview of the LHCb experiment, with a special focus on the upgrade of the detector that is planned for the Long Shutdown 3 (LS3, 2024-2026) to face the High-Luminosity phase of the LHC (HL-LHC) that will begin after the Long Shutdown 4 (LS4, 2030).

2.1 The Large Hadron Collider (LHC)

The Large Hadron Collider is the world's largest and most powerful particle accelerator located at CERN. It first started up on 10 September 2008, and remains the latest addition to CERN's accelerator complex.
The LHC consists of two 27-kilometers rings of superconducting magnets alternating with a number of accelerating cavities to boost the energy of the particles along the structure. It is installed 100m underground at the Franco-Swiss border near Geneva, in the tunnel that until 2000 hosted the *Large Electron Positron* (LEP) collider.
Inside the accelerator, two high-energy particle beams travel in opposite directions close to the speed of light before they are made to collide.
The main operation mode of LHC is represented by proton-proton (pp) collisions at the centre of mass energy of $\sqrt{s} = 13$ TeV, which is near the maximum designed value of 14TeV.

The Large Hadron Collider was commissioned in 2010 for proton–proton collisions with a 7 TeV centre-of-mass (c.o.m.) energy. It delivered 8 TeV c.o.m. proton collisions from April 2012 until the end of Run 1 in 2013, and it was operated with 50 ns bunch spacing. After some consolidation measurements performed during the Long Shutdown 1 (LS1) in 2013–2014, the LHC was operated in Run2 at 13 TeV c.o.m. proton collisions from 2015 until the end of 2018, with a bunch spacing reduced to 25 ns, reaching a peak luminosity of $2 \times 10^{34} cm^{-2}s^{-1}$, which is twice the nominal design value. During 2020 LHC was in Long Shutdown 2 (LS2), and as a consequence of the coronavirus pandemic, LS2 will lasted almost one year longer than foreseen, with Run 3 now planned to start at the during 2022.

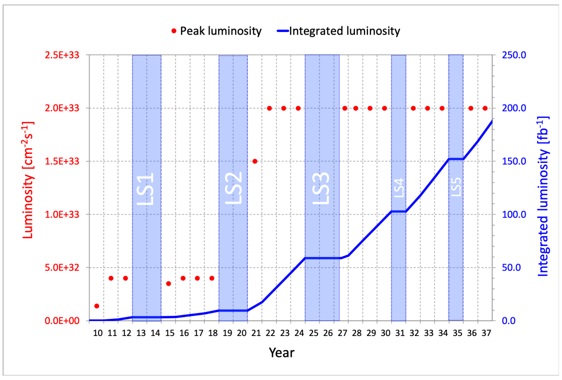

Figure 2.1: LHC luminosity plan from 2010 to 2038. The blue line represents the integrated luminosity measured or predicted. The red dots represent the measured or predicted instantaneous luminosity.

2.1.1 High Luminosity LHC

To sustain and increase the discovery potential of LHC, the Large Hadron Collider will need a major upgrade during the 2020s, firstly to extend its operability by another decade or more, and secondly to increase its collision rate and thus the integrated luminosity. The new configuration, known as *High Luminosity LHC (HL-LHC)* pushes the accelerator technology beyond its present limits. More in detail, the target established by CERN in the high-luminosity LHC project at the end of 2010 is to increase the instantaneous luminosity by a factor of five beyond the original design value, with a peak luminosity of $5 \times 10^{34} cm^{-2}s^{-1}$, and the integrated luminosity by a factor ten (250 fb^{-1} per year). Luminosity is an important indicator of the performance of an accelerator: it is proportional to the number of collisions that occur in a given amount of time. The higher the luminosity, the more data the experiments can gather to allow them to observe rare processes.
Therefore the LHC systems will need to be changed, and possibly improved, because they either become vulnerable to breakdown and accelerated aging, or because they may become a bottleneck for operation at higher performance levels and in a higher radiation environment.

The High-Luminosity LHC, which should be operational from the beginning of 2029, will provide more accurate measurements of new particles and enable the observation of rare processes that occur below the current sensitivity level. This will make it possible to detect rare events not previously witnessed, and increase our understanding of the energy frontier.

2.2 The LHCb detector

The LHCb detector is a single-arm forward spectrometer with a forward angular coverage from approximately 10 mrad to 300 (250) mrad in the horizontal (vertical) plane, corresponding to a pseudorapidity η range $2 < \eta < 5$ in the forward direction. It represents an experiment dedicated to heavy favour physics at the LHC, designed for the study of particles containing b or c quarks. Its primary goal is to look for indirect evidence of new physics in CP violation and rare decays of beauty and charm hadrons.

The peculiar geometry of the LHCb detector, compared to the typical design of the general purpose detectors at CERN, is motivated by the fact that in proton-proton collisions at the LHC energy scale the $b\bar{b}$ hadron pairs are mainly produced at small polar angles with respect to the beam direction both in the forward and backward direction.

The layout of the detector shown in Figure 2.2 includes a high-precision tracking system, two-rings imaging Cherenkov detectors, a calorimetry system and a muon detector. The coordinate system adopted has the origin in the interaction point, with

- the x-axis is along the horizontal, pointing from the origin towards the outside of the LHC ring
- the y-axis perpendicular to the x-axis and the beam direction, with an inclination of 3.601mrad with respect to the vertical.
- the z-axis aligned with the beam direction

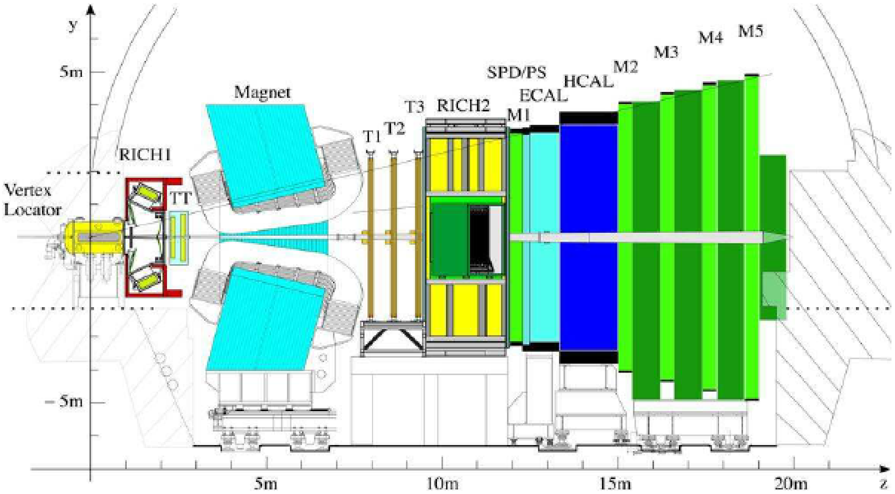

Figure 2.2: Lateral view of the LHCb detector.

The tracking systems consists of a silicon-strip vertex detector surrounding the *pp* interaction region, a large-area silicon-strip detector located upstream of a dipole magnet with a bending power of about 4 Tm, and three stations of silicon-strip detectors and straw drift tubes placed downstream. For hadrons identification two ring-imaging Cherenkov (RICH) detectors are used, while muons are identified by a system composed of alternating layers of iron and multiwire proportional chambers. One of the main components of the LHCb detector is the electromagnetic calorimeter (ECAL), which provides the identification of electrons and photons and the measurement of their energies and positions. For hadrons, the same function is performed by a hadronic calorimeter (HCAL). The trigger consists of a hardware stage, based on information collected from the calorimeter and muon systems at a rate of 40 MHz, called ”L0 trigger”, followed by a software stage, which applies a full event reconstruction, known as the ”High Level Trigger” (HLT).
The next sections will better describe the LHCb electromagnetic calorimeter and its layout designed for the Upgrade I and II of LHCb.

2.3 ECAL

One of the main components of the current LHCb detector is the ECAL, a sampling calorimeter which actually is made of Shashlik modules, forming a $7.76 \times 6.30 m^2$ wall developed in the forward region.

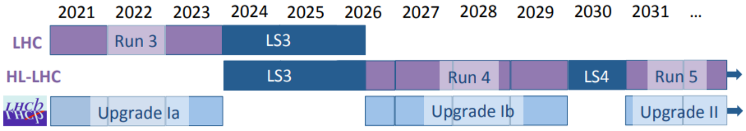

Figure 2.3: Timeline of accelerator and experiment operations over the decade 2021 to 2031, including both the periods of operations of the LHC and HL-LHC and the long shutdowns (LS).

As mentioned in the paragraph 2.1.1, LHC will undergo a major upgrade to enter the High Luminosity phase, therefore the LHCb collaboration proposed an Upgrade II to be installed during the Long Shutdown 4 (LS4) in 2030.
The project for the LHCb detector Upgrade II will be built on the achievements of the current detector, which is the result of the Upgrade I. New attributes will also enhance the detector’s capabilities to a wider range of physics signatures. This upgrade will allow the experiment to accumulate data corresponding to a minimum of 300 fb^{-1} , enable many important observables to be measured with a precision unattainable at any other experiment, and in addition it will extend the HL-LHC’s capabilities to search for physics beyond the Standard Model (SM).

2.3.1 ECAL Upgrade I

The actual LHCb ECAL has a sampling structure based on Shashlik-type modules with a transverse dimensions of $12 \times 12cm^2$. The modules are constructed from alternating layers of 2 mm thick lead tiles, and 4 mm polystirene scintillating plates.
When particles hit the metal plates, they produce showers of secondary particles. These, in turn, excite the plastic material, which emits ultraviolet light. The calorimeter then provides the energy loss measurements from the amount of UV produced, which is proportional to the energy of the particles entering the calorimeter. The scintillation light is collected and transported by wavelength-shifting fibres to photomultiplier tubes (PMT) mounted on the back.

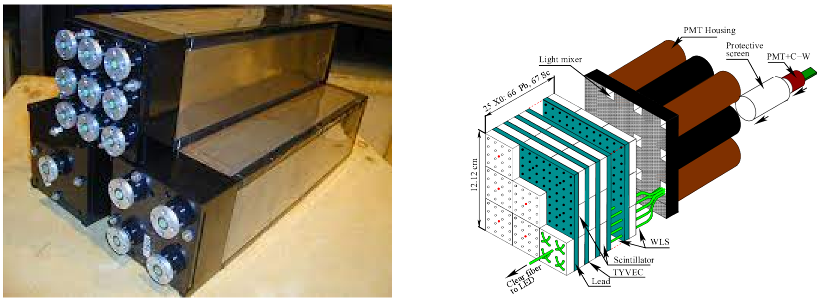

(a) (b)

Figure 2.4: Shashlik module scheme.

The assembly results in a energy resolution with a 10% sampling and a 1% constant term. In order to keep the occupancy below 10%, the calorimeter is divided into three regions with three different granularities, namely a $4 \times 4cm^2$ inner region, a $6 \times 6cm^2$ middle region and a $12 \times 12cm^2$ outer one. A critical parameter of the ECAL is the radiation tolerance. The radiation tolerance of the Shashlik modules has undergone in-depth studies through irradiation campaigns, concluding that 40 kGy is the operational limit, which will be reached by the modules in the innermost region by LS3.

Shashlik Modules The ECAL employs Shashlik technology of alternating scintillating tiles and lead plates. The cell size varies from 4 x 4 cm in the inner part of the detector, to 6 x 6 cm and 12 x 12 cm in the middle and outer parts. The overall detector dimensions are 7.76 x 6.30 m, covering an acceptance of $25mrad < \theta_x < 300mrad$ in the horizontal plane and $25mrad < \theta_y < 250mrad$ in the vertical. Light is detected by 10-stage photomultipliers (Hamamatsu R7899-20) with an individually regulated high voltage base of Cockcroft-Walton type.

2.3.2 ECAL Upgrade II

For the Upgrade II of LHCb experiment, which is proposed during the LS4 of LHC, the upgraded detector will operate at a maximum luminosity of $1.5x10^{34}cm^{-2}s^{-1}$. Firstly,

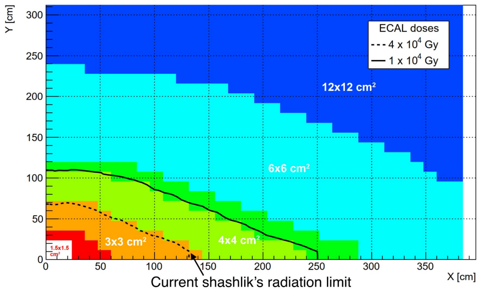

Figure 2.5: First optimisation of ECAL regions and cell sizes for Upgrade II with the SpaCal/Shashlik option.

the radiation environment will be extremely severe, with a total dose of around 1 MGy foreseen for the innermost modules. Indeed, a significant degradation in performance is already expected for these modules in the innermost region of the detector by the time of LS3. Therefore the LHCb ECAL system and will need to be modified, and possibly improved to operate at higher performance levels and in a higher radiation environment. A major change will have to be introduced in its design and in the choice of materials for its upgrade.

The baseline option for the upgraded calorimetry combines the existing Shashlik technology in the outer region with a new technology in the central region, where the accumulated dose is expected to exceed 40 kGy. The most severe requirement of >200 kGy radiation tolerance can be met by crystal fibres, leading to a so-called Spaghetti Calorimeter (SpaCal) in the central region. It consists of a dense absorber with rows of holes in which an active medium acting both as scintillator and light-transporting medium is inserted. This configuration introduces flexibility in defining the cell size as the area over which the fibres are read out. Presently, a solution being investigated is to introduce new radiation hard materials in the detector setup to face the high doses and to insert two additional inner regions to increase the granularity, namely a 1.5x$1.5cm^2$ and a 3x$3cm^2$ regions with 32 and 144 modules respectively.

For the innermost region a first prototype was built out of a W absorber (SPACAL WGAGG), equipped with Garnet crysral fibres (YAG, GAGG), while for the other region another module with a Lead absorber and Polystyrene fibres has been set up (SPACAL Pb).

The high occupancy in the central region motivates splitting the SpaCal modules longitudinally in two sections at around the shower maximum. A double readout is then used to achieve the best possible timing and to improve clustering reconstruction and particle identification. The algorithms exploit the fact that the showers are less developed in the upstream section, meaning that the front readout suffers less from pile-up, while the timing in the back section helps clusterisation over adjacent cells. Studies also show that the longitudinal segmentation makes the SpaCal performance more robust against radiation damage.

Moreover, given the increased luminosity, a higher event rate is expected and also the high number of candidates in every event will lead to a large combinatoric background. Therefore to reduce these effects the the idea is to provide the whole calorimeter with a precise timing information, of the order of a few tens of picoseconds, while keeping the energy resolution at least as the current one. Time information provided by the tracking detectors will also help the association of electromagnetic clusters to charged-particle tracks and primary vertices. There is also a variation of the option described above, which consists of combining the Shashlik/SpaCal detector configuration with a dedicated timing layer inserted between the back and front sections of the modules at around the shower maximum. Future investigation on the limits of both the SpaCal and Shashlik timing performance will determine whether a timing layer may bring benefit over the whole ECAL.
In addition, a smaller Molière radius will be of benefit to the reconstruction algorithm, reducing the occupancy and the background noise. Since the calorimeter is a sampling type, it is possible to tune the R_M radius by combining different materials in the absorber according to their density, or varying the distance between the fibres and their section to provide the required performances in terms of both spatial and energy resolution.

The baseline goal of the ECAL for Upgrade II is to solve the above challenges and provide a performance that is at least as good as that of the current detector in Run 1 and Run 2 conditions. The main challenges in designing an electromagnetic calorimeter for Upgrade II consist in achieving an energy resolution and reconstruction efficiency similar to the original detector at a significantly higher pile-up and overall occupancy, with a radiation tolerance that is compatible with an accumulated dose corresponding to 300 fb^{-1} of integrated luminosity.

2.3.3 SpaCal Prototypes

A SpaCal is a sampling calorimeter wherein scintillating fibres are inserted into a dense absorber. The scintillating fibres convert the energy deposited into light and transport it to the photodetectors. This avoids the need of wavelength-shifters which entail a reduction in light collection efficiency and consequently time resolution. At the same time, the electromagnetic shower dimension can be tuned selecting absorber materials with adequate radiation length and Molière radius. Moreover, the choice of the crystal and polystyrene fibres was justified by their scintillation properties, high density and a big index of refraction favouring Cherenkov production.
As already mentioned, there are two promising prototypes designed for the $1.5 \times 1.5 cm^2$ and the $3 \times 3 cm^2$ regions. For the innermost region a first prototype was built out of a W absorber, equipped with Garnet crysral fibres (YAG, GAGG), while for the other region another module with a Lead absorber and Polystyrene fibres has been set up. They are called *SpaCal WGAGG* and the *SpaCal Pb* respectively.
These prototypes share some properties. For instance they are both longitudinally segmented into two sections, called front and a back section, to match the crystals' length and each part is additionally divided into nine cells. To decouple front and back sections

and extract more light from the cells, a thin layer of a reflective material is installed in the gap.
Positioned in front of almost all cells there is a plexiglass light guide, shaped in a truncated-pyramidal geometry with beveled edges, and dry coupled to a Hamamatsu photomultiplier tube (PMT), which provides the electronics readout of the signal. At the end, for the test beam setup also a LED system is installed in the prototypes: each section has a total of four LEDs which are positioned such that the PMTs receive approximately the same amount of light.

Spacal W-GAGG : The active part of the SpaCal W-GAGG prototype is made of Garnet crystal fibres, which due to the constraints imposed by the maximum available ingots dimension, are cut 100 mm long with a $1mm \times 1mm$ square section.

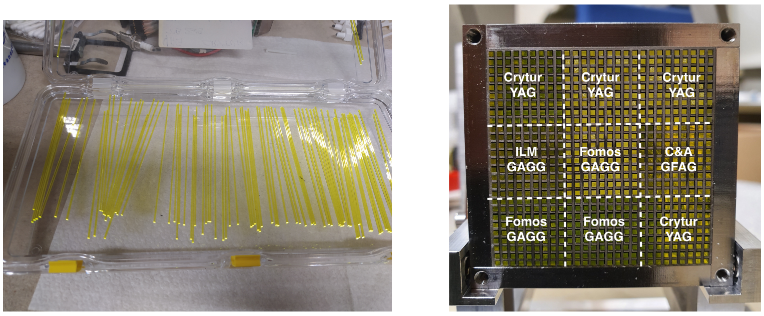

(a)

(b)

Figure 2.6: Left: GAGG crystal fibres $1mm \times 1mm$ square section. Right: SpaCal W-GAGG frontal view, with a scheme of the 9 cells and the name of the scintillating material employed in each cell.

The absorber is made of pure Tungsten plates 0.5 mm thick and 19 g/cm^3 dense that form a grid of rows with squared holes of 1.2 mm side, wherein the fibres could be inserted. Consequently, the pitch between holes is 1.7 mm. The absorber is longitudinally segmented into a front section 40 mm long and a back one 100 mm long. Assuming a theoretical radiation length X_0 of 6 mm, the first section corresponds to almost $7X_0$, which corresponds to the position of the shower maximum for 20 GeV electrons. Each section has its own read out on one side and a 2 mm thick stainless steel plate on the opposite side. Then a thin foil of reflective material (viquity) lies between the plate and the fibres to redirect light towards the readout side.

The scintillating fibres are Cerium-doped garnet crystals, namely $Gd_3Al_2Ga_3O_{12}$ (GAGG) and $Y_3Al_5O_{12}$ (YAG), that were chosen for for their radiation hardness and to achieve the best timing resolution out of a characterisation campain involving different producers. First, GAGG is intrinsically faster and brighter than YAG thanks to Gallium, which reduces the band gap thus burying electronic shallow traps in the conduction band. Secondly, GAGG is denser, which increases stopping power and the sampling fraction of the

calorimeter.
Each section of the prototype was equipped with 1 cell of GFAG from C&A (Japan), 1 of GAGG from Institut Lumière Matière (ILM, France), 3 of GAGG from Fomos (Russia), and the remaining 4 with YAG fibres from Crytur (Czech Republic). The fibres were positioned to have the same arrangement in the front and back section.
The prototype was read out with two sets of photomultipliers tubes (PMTs) Hamamatsu, the R12421 was employed for the energy resolution, while the R14755U-100 for time measurements.

Figure 2.7: Hamamatsu R12421 PMT employed for the readout of SpaCal W-GAGG prototype

The R12421 PMTs are cylindrical with a diameter shorter than 15 mm, thus allowing 9 of them to be placed next to each other and to read out all the cells at the same time. The R7600U-20 PMTs are optimised for precise timing. They feature metal channel dynodes (MCD), which are extremely thin electrodes in close proximity to each other. This technology ensures better time resolution due to the short path and small spatial spread of the electronic cloud. On the other hand their lateral dimensions ($30mm \times 30mm$) do not allow for a full coverage of the module, so only one cell at the front and one at the back was equipped with these PMTs.

Spacal Pb-Polystyrene : The active part of the SpaCal Pb-Poly prototype is made of cylindric Polystyrene fibres with $1mm$ diameter and with a pitchof 1.7 mm.

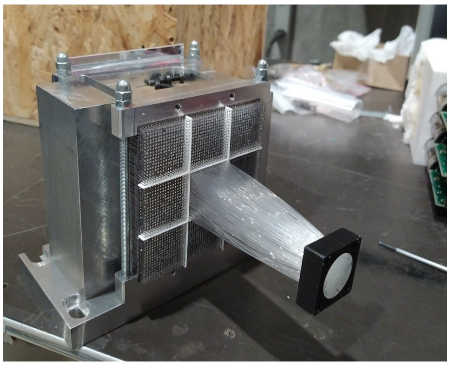

Figure 2.8: Front section of the SpaCal Pb prototype.

The absorber in this case is made of lead and it is longitudinally segmented into a front section 80 mm long and a back one 210 mm long such that the gap corresponds to the position of the shower maximum for 20 GeV electrons. As for the SpaCal W, each section has its own read out and a thin foil of viquity placed between the two sections.

The central cell of front section of the prototype was equipped with a fibres bundle to test different light collection techniques, while in the others, the fibres were positioned to have the same arrangement in the front and back section.
The prototype read out is provided by two sets of photomultipliers tubes (PMTs) Hamamatsu, the R7899-20 employed in the beam test at SPS in november, which are the standard for the LHCb ECAL, and R11187 (TILECAL) used at DESY test beam.

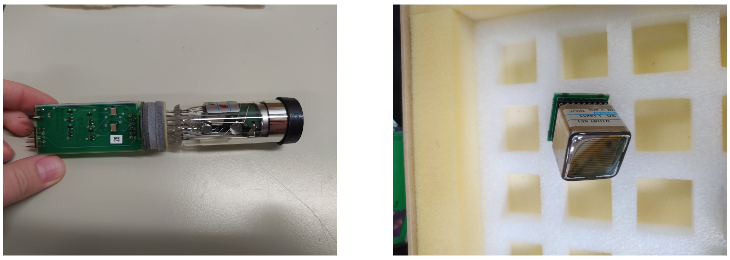
(a) (b)

Figure 2.9: Left: PMT Hamamatsu R7899-20 for the beam test at SPS. Right: PMT Hamamatsu R11187 for the beam test at DESY.

The prototype assembled is a SPACAL with a pure Tungsten absorber and garnet crystal fibres (Fig. **??**). It is longitudinally segmented into a front and a back section close to the average shower maximum. The two were made independent to allow inserting a large area picosecond photodetector (LAPPD) as an optional timing layer between the two, discussed in [**?**].

Each section is divided into 9 cells of 15×15 mm^2 surface, read out by photomultipier tubes (PMT) discussed in the measurements sections.

2.3.4 Energy Resolution

As mentioned in Section 1.2, one of the most important task of a calorimetry system is the energy measurement and the precision which this is done, known as energy resolution. To determine this fundamental property, the Shashlik modules and other prototypes have undergone extensive test campaigns with electrons at DESY in the range 1 5.8 GeV and at CERN up to 120 GeV.

The results obtained for the energy resolution are the ones shown in Figure 2.10, from which it can be concluded that the energy resolution obtained from the test-beam results is slightly worse with respect to the values expected from MC simulations. However the sampling term for both SpaCal and Shashlik prototypes is around $10\%/\sqrt{E}$. Also, the performance of SpaCal worsens at small incidence angles as a result of differences in the

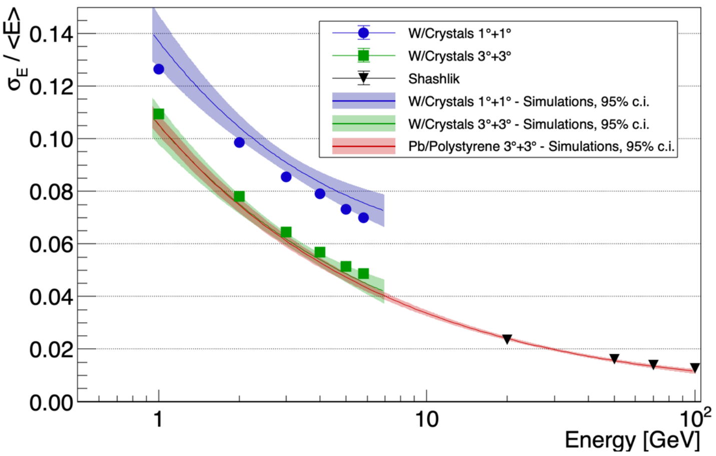

Figure 2.10: Energy resolution for SpaCal W/GAGG and Pb/PS modules oriented at 3 ○ +3 ○ with respect to the beam axis and for a Shashlik module, as measured in test beam. For comparison, the energy resolution for a SpaCal W/GAGG module oriented at 1 ○ + 1 ○ with respect to the beam axis is also shown (Picture from [6]).

sampling and longitudinal fluctuations depending on whether the particle first enters into a fibre or the absorber. To moderate this effect, it is envisaged to orient the modules at an angle of a few degrees with respect to the LHCb beam axis.

2.4 Requirements for SpaCal Prototypes

For the Upgrade II of the ECAL, the idea is to provide the whole calorimeter with a precise timing information, of the order of a few tens of picoseconds, while keeping the energy resolution at least as the current one. At the same time the spatial resolution should reach values around 1 mm. This level of precision would guarantee first an efficient separation of the overlapping showers, and secondly a precise reconstruction of the position for both neutral and charged particles. For the charged ones, the signals in ECAL are matched with the trajectories reconstructed from the tracking detector to perform an accurate particle identification. As for the neutral particles, the position measurement is only available from the calorimeter, and it is fundamental to reconstruct events.
Also a good angular resolution is required for the Upgrade II of the ECAL to study theories with physics beyond the Standard Model that involve particles with a detectable decay length from the interaction point, known as Long-Lived Particles (LLP). Up to now, among the tracks reconstructed in LHCb, long-lived particle searches employed only long tracks which combine the information of all the tracking subdetectors. For instance, a way to detect LLP is through leptonic or semileptonic decay mode, triggering on μ or e^- displaced vertex far from the interaction point. This decay could take place after the

inner tracker, inside the electromagnetic calorimeter. Therefore, providing the ECAL with a good angular resolution, would be of benefit to match the information with the ones coming from the tracker for the LLP reconstruction.

Chapter 3

Test-Beam Setup and Analysis

The aim of this thesis is to investigate the performances of the SpaCal prototypes in terms of the angular and spatial resolution, which are strictly correlated to each other. To do so, the modules were tested at SPS and DESY facilities, with different energies and configurations.
In this chapter, a detailed description of the setup used during the Beam Tests is presented and followed by an introduction to the procedure to perform the analysis of the experimental measurements and the Monte Carlo simulation outcomes.

3.1 Test-Beam Setup

The prototype was mounted on two steppers rotating along the azimuthal and the altitude directions, that allow the module to be tilted. For instance, a rotation of 3° along both directions will be indicated with the notation 3°+3° from now on. Then the assembly was placed inside a black box, and aligned with the beam thanks to the moving table on which the box was installed.

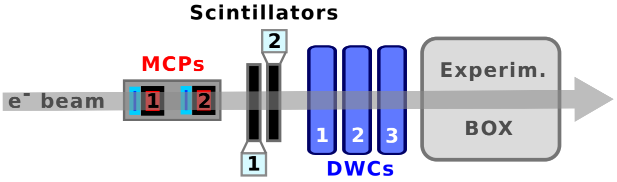

Figure 3.1: Beam Test setup at SPS.

Different components were employed in the acquisition during the Beam Test, The setup shown in Figure 3.1 consisted of

- two **MicroChannel Plate** detectors (MCP-PMTs) for the time reference, with a combined time resolution of ∼15 ps
- two **Scintillator** counters in coincidence acting as a hardware trigger

- three **Delay Wire Chambers** (DWCs) employing a mixture of Ar/CO_2 (80% Ar, 20% CO_2) gas for the tracking information, which provide the position of the incoming beam particles along x and y directions with a precision of $\sim 200\mu m$.

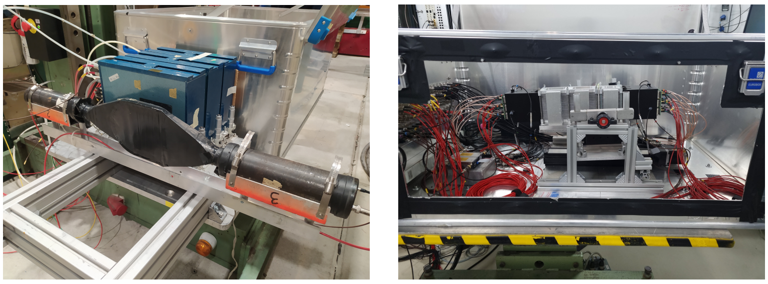

Figure 3.2: Beam Test setup at SPS. Left: scintillating pads (black) and DWCs (blue) put in front of the box where the prototype is installed. Right: SpaCal Pb prototype installed on the stage inside the box, rotated of 3°+3°.

The amplitude measurements in the module channels were performed with three ADC LeCroy 1182 VME Charge-to-Digital converters, with a 400 ns gate.

3.2 Spatial Resolution

The position of the incident particle is usually obtained using the method of the *Center of Gravity (COG)* of the electromagnetic shower with some additional corrections as previously explained in the Section 1.3.
The general idea is to compare the position in x and y measured by the DWCs with the COG coordinates of the shower (x_{cog}, y_{cog}), both projected onto the surface of the front section of the prototype under examination (see Figure 3.3). Before performing the projection, the longitudinal barycenter of the shower should be evaluated at a given energy with the L-correction expressed in the Equation 1.11. The two parameters p_0 and p_1 are extracted from MC simulation with the procedure explained in the Section 4.1.2. On the other hand, the transversal COG (x_{cog}, y_{cog}) is evaluated as the energy-weighted barycenter of the cluster normalized by the cellsize, which is equal to 15.3 mm for the SpaCal W and 30.6 mm for the SpaCal Pb.

$$x_b = \frac{1}{cellsize}\frac{\sum_{i=1}^{9} x_i E_i}{\sum_{i=1}^{9} E_i} \qquad y_b = \frac{1}{cellsize}\frac{\sum_{i=1}^{9} y_i E_i}{\sum_{i=1}^{9} E_i} \tag{3.1}$$

The quantity E_i corresponds to the energy deposited in the cell i, and x_i, y_i are the x and y position of the centre of that cell. Then, using the Equation 1.12 the transversal barycenter is corrected for the non linear profile of the shower along the direction perpendicular to the beam. The S-correction expresses the S-shaped relation between the centre of gravity of the cluster and the DWC's coordinates system shown in the Figure

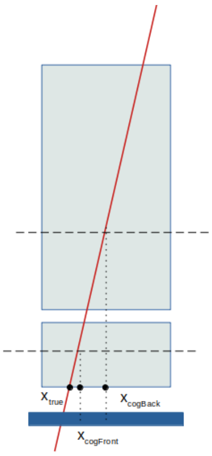

Figure 3.3: Projection of the DWC's coordinates and the COG of the shower on the front surface of the prototype.

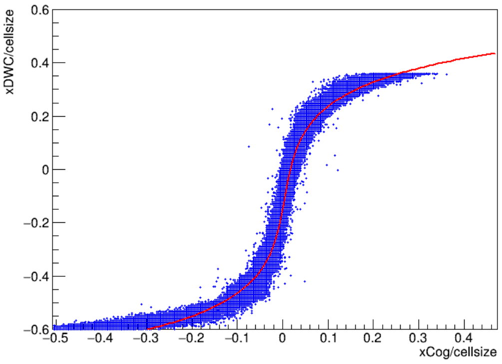

Figure 3.4: Example of S-shaped relation between the x COG coordinate evaluated in the front section and the x position of the beam particle measured by the first DWC.

3.4.
Afterwards, the direction of flight of the particle was obtained with good accuracy starting from the positions measured by the DWCs. Once the track is reconstructed, it was possible to project the points on a certain surface. The following step consisted on the projection of the DWC's coordinates and the COG ones on the z plane corresponding to the front surface of the module.
Before the spatial resolution is evaluated, some filters needs to be applied to the datasets to clean the beam. The plot in Figure 3.5, for instance, shows x and y ranges divided into bins, where the colour scale represents the integrated charge produced by the interaction of the beam particles with the prototype in that part of the cell. The yellow square region in the middle represents the events in which the particles hit the centre of the cell of interest. However, since the beam was wide enough to cover a big portion of the

prototype, there are also particles that do not hit the cell we wanted to analyse.

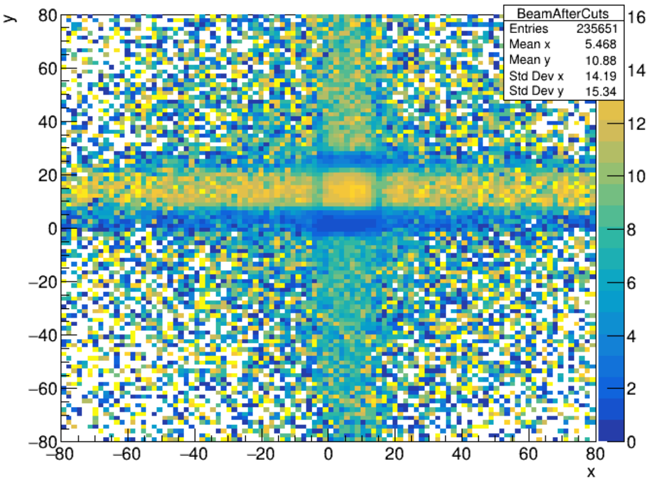

Figure 3.5: Profile of the beam intensity for the SpaCal W: x and y coordinate (mm) along the x and y axis; the intensity of the beam seen by the central cell is expressed in a colour scale without any filter.

So first of all, the cuts on the position along x and y were set such that only the central cell for both front and back section was selected.

Also, some additional filters were applied.

DWCs Correlations: the three DWCs employed in the test-beam setup provide the measurement of three coordinates along x (x_0, x_1, x_2) and three along y (y_0, y_1, y_2). Since the three coordinates measured along the same direction belong to the same particle trajectory, they are expected to be correlated, i.e. their relation should follow a diagonal distribution. For instance, x_0 obtained from the first DWC and x_1 from the second one, are connected by a linear function, as shown in Figure 3.6.

However, there are additional signals distributed as a cross sing and a halo that appears around 0. In principle, this could be associated with the particles that start to shower before entering the prototype. Therefore, it is essential to put filters on the correlation plots in order to correct for this effect and the noise and to select only those events in a close region around the diagonal for which a correlation between the two chambers is observed.

Total Energy: the total energy deposited is obtained by the sum of the deposition in the front and in the back section, and it is well described by a gaussian distribution. To be sure that random events not associated to beam particles are not considered, selected events are those that lie within the gaussian mean $\pm 2\sigma$.

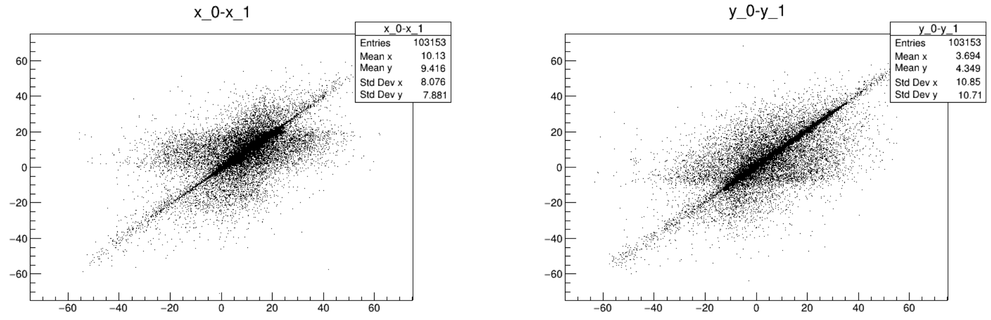

(a) (b)

Figure 3.6: Left: correlation between the x position measured by the first and the second DWC. Right: correlation between the y position measured by the first and the second DWC.

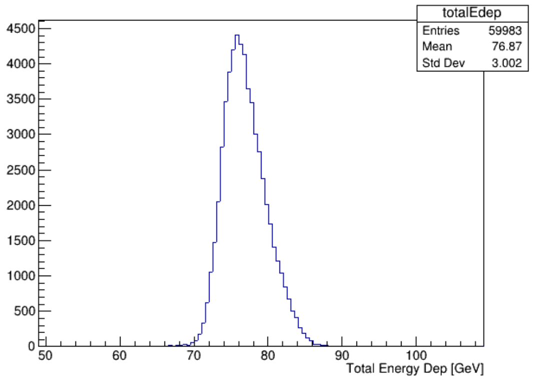

Figure 3.7: Example of the distribution of the total energy deposited in the front and in the back section without any filter.

Angular Distribution of the Beam: to understand the angular distribution of the beam, a tracking code was implemented. The position of the particle is measured by the DWCs along x and y directions, while the z coordinates are fixed in correspondence where the chambers were installed. The tracking implementation allows to reconstruct the trajectory of the particles using these informations, by fitting with a linear function the relation between z and x (or y) coordinates. Therefore the direction of the particle can be extrapolated from the angular coefficient of the linear function p_1.
The angular distribution of the beam ϕ shown in Figure 3.8 is obtained by

$$\phi = atan(p_1) \tag{3.2}$$

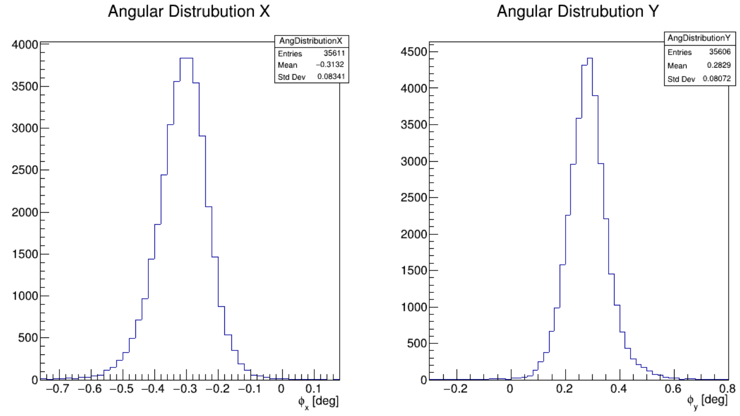

Figure 3.8: Example of the angular distribution of the beam in x and y directions.

Before applying filters on the angular distribution, a check on the stability of the angle of the beam and on its spread was performed throughout the runs.

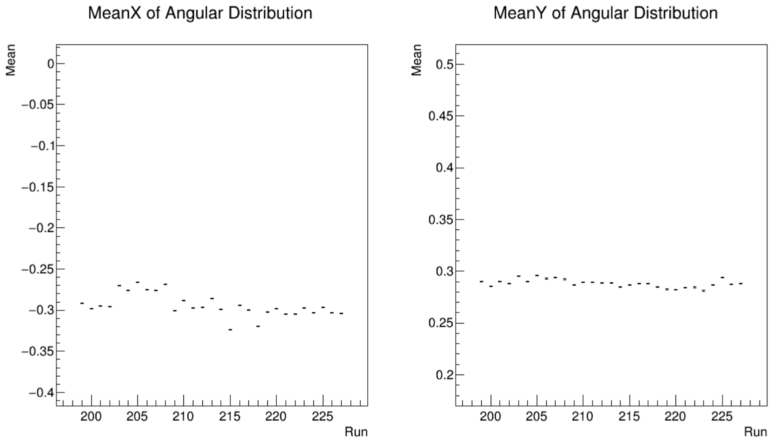

Figure 3.9: Mean value of the angular distribution of the beam throughout the runs.

From the plots shown in Figure 3.9 it can be noticed how the mean angular distribution remains stable within some fluctuation throughout the runs, which are made at different angles and energies. Indeed, the position measured by the DWCs do not change even if the module is rotated. Then the angle of the beam with respect to the DWC xy plane is the offset of the plot, which corresponds to -0.3° for x and 0.3° for y. Indeed the position measured by the DWCs do not change even if the module is rotated.
Also the trend of the σ is more or less constant around the same value, with some fluctuations, as shown in Figure 3.9.

Once all the filters are applied, the spatial resolution can be evaluated starting from the difference between the S-corrected coordinates and the true position measured by the

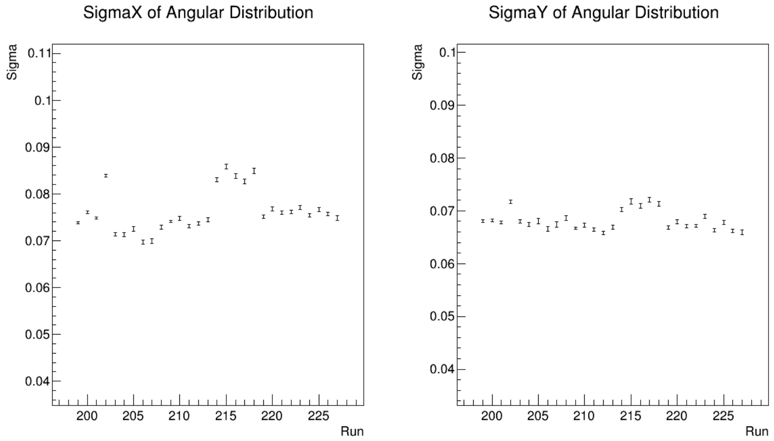

Figure 3.10: Spread of the angular distribution of the beam throughout the runs.

DWCs. This quantity should follow a gaussian distribution centered in 0 and normalised by the cellsize. Once this property is checked, the *Spatial Resolution* is obtained by multiplying the σ of that distribution by the cellsize.

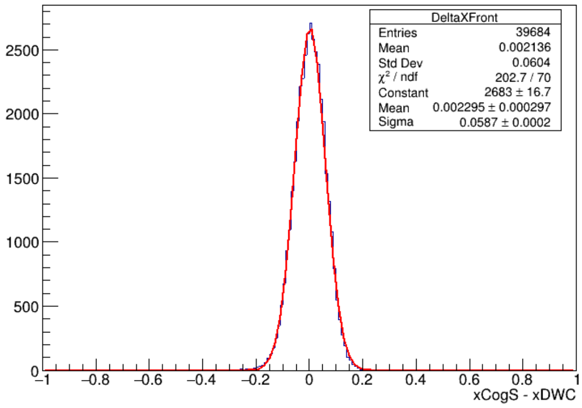

Figure 3.11: Example of the gaussian distribution of the difference between the S-corrected COG coordinate along x and the x position measured by the first DWC.

The position resolution evaluation for the front and the back section separately, gives the barycenter of the part of the shower that has deposited energy in a single section only. In order to estimate the SpaCal position ability, the overall barycenter of the shower that develops inside the prototype needs to be performed. Combining the information of the two longitudinal sections can improve further the spatial resolution of the module.
In my thesis I studied 2 combination methods, considering the x and y direction indipendently. The first involves the use of the *standard average* between the front and the back

to get the overall spatial resolution along x and y (σ_x, σ_y).

$$x_{cog} = \frac{x_{cogBack} + x_{cogFront}}{2} \qquad y_{cog} = \frac{y_{cogBack} + y_{cogFront}}{2} \tag{3.3}$$

In this case $x_{cogFront}, x_{cogBack}, y_{cogFront}, y_{cogBack}$ correspond to the S-corrected coordinates of the transverse centre of gravity in the specified section of the prototype. Once the combined COG are evaluated with Equation 3.3, the spatial resolution is evaluated from the difference between these values and the true positions measured by the DWCs projected to the same z plane as the σ of that distribution multiplied by the cellsize.
On the other hand, it is possible to combine the two sections with the *weighted average* of the front and back section expressed in Equation 3.4,

$$x_{cog} = \frac{x_{cogBack}/\sigma^2_{xBack} + x_{cogFront}/\sigma^2_{xFront}}{\frac{1}{\sigma^2_{xBack}} + \frac{1}{\sigma^2_{xFront}}} \qquad y_{cog} = \frac{y_{cogBack}/\sigma^2_{yBack} + y_{cogFront}/\sigma^2_{yFront}}{\frac{1}{\sigma^2_{yBack}} + \frac{1}{\sigma^2_{yFront}}} \tag{3.4}$$

where the weights correspond to the spatial resolution of the respective section at a given energy, obtained by considering the front and back separately, and the sigma of the the x_{cog} and y_{cog} distribution is evaluated to determine the resolution from this method.

3.3 Angular Resolution

To investigate the angular resolution of the prototypes, which is strictly correlated to the position resolution of the particle, the SpaCal W and the SpaCal Pb were rotated along the azimuthal and the altitude directions, so that the beam particles arrived on the surface at a θ angle. This quantity can be calculated geometrically from the SpaCal information as the angle between the vertical axis of the prototype and the particle trajectory, as shown in Figure 3.12.

$$\theta = atan\left(\frac{x_{cogBack} - x_{cogFront}}{z_{cogBack} - z_{cogFront}}\right) \tag{3.5}$$

The θ angle is then expressed in Equation 3.5, where $z_{cogBack}$ and $z_{cogFront}$ are the mean of the energy deposition histograms along the z axis for the front and the back section, extrapolated from Monte Carlo simulations. Instead x_{Back} and x_{Front} are the projection of the COG into the DWC's coordinates system.
To perform the projection the S parameters of the Equation 1.12 were set to the values obtained when the prototype was not rotated. Then this S-function was used to calibrate and correct the data.
At the end the θ angle follows a gaussian distribution, and the angular resolution in radians is obtained as the σ of that distribution.

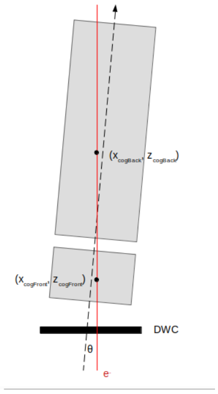

Figure 3.12: Configuration of the prototype and the first DWC with a rotation angle θ along x or y direction. The red line represents the electron/positron beam, the black dot line instead is the symmetry axis of the SpaCal prototype under examination.

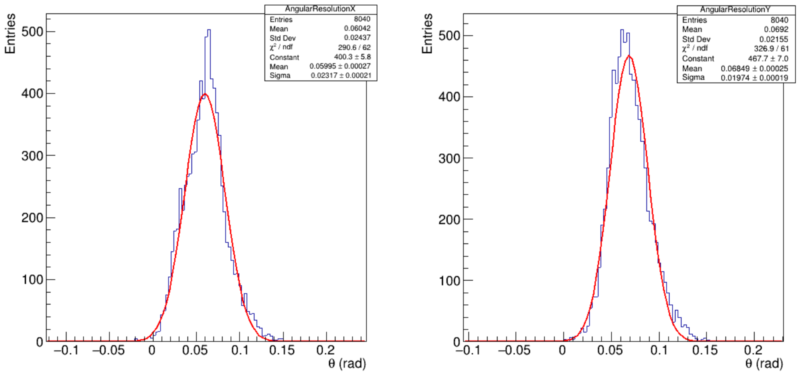

Figure 3.13: Example of the θ distribution with a gaussian fit along x (left) and y (right) direction.

Chapter 4

Monte Carlo Simulations with SpaCal Prototypes

In this chapter, the beam test configuration presented in Section 3.1 is reproduced with Monte Carlo (MC) simulations to study the spatial resolution of the SpaCal W and SpaCal Pb prototypes, as it was done with the test-beam data. The same beam energies for the electrons were investigated, with a 3° rotation along the azimuthal and the altitude directions for both modules.
A single 3×3 module, shown in Figure 4.1 is defined in a configuration file and reproduced with GEANT4, a simulation software that reconstructs how the radiation interacts with the detector medium and evaluates the energy deposition of the particles in the module of the calorimeter. Since the PMTs and the light guides are not included in the configuration, there are no real readout channels: basically, a cell is the fundamental unit of the readout chain. Essentially, a cell is just a collection of holes in an absorber that are filled with crystals with some air gaps.

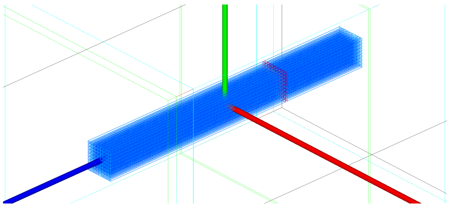

Figure 4.1: Example of the simulation of the SpaCal W prototype with the single 3×3 module.

The simulations consists of different steps, starting from the definition of the particle source and its properties. The idea is to shoot a squared beam of electrons with various sections. The beam is directed with the desired stereo angle on the target, defined as the center of the central cell. More specifically, the beam target is chosen in such a way that the beam main axis crosses the xy center of that cell when z is at the front/back separation. In this way, a good lateral containment of the shower in the module is guaranteed.

Then GEANT4 handles the interaction of the electrons with the module, reproducing a map of the full energy deposition within the detector. The next step is the optical calibration based on the energy deposition, that characterise the expected optical photons output through a scan of the crystal on a space grid. This provides a map of extraction efficiency and the arrival time distribution as a function of fibre position.
In principle, ray tracing of optical photons could be useful to study in detail the performance of the prototypes. Nevertheless this method requires too much CPU time. The simulation type that in this case defines the propagation of the scintillation photons in the active medium is then the hybrid MC, that maintains a good level of realism while keeping the simulation faster.
The hybrid simulation uses the maps created by GEANT4 and the energy deposition to calculate the number of photons generated and their arrival time on the PMTs. Starting from these information, the quantum efficiency of the PMTs is simulated and actual pulses can be produced.

From the MC simulation output one can extract some information for each event about the total number or photons detected, which is useful to understand the total amount of energy deposited. Also, an array for each cell is produced, and it contains the simulated and digitised pulse. An example of the output signal produced by the central cell of the front section is shown in Figure 4.2.

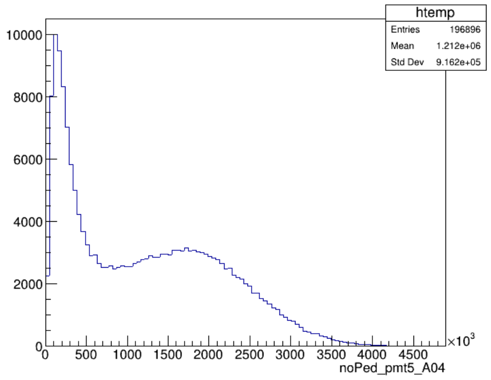

Figure 4.2: Output signal of the PMT connected to the cell number 5 of the SpaCal W, tested with 40 GeV electron source.

4.1 Monte Carlo Simulations Analysis

The analysis to obtain the spatial resolution of the SpaCal prototypes follows the procedure explained in Section 3.2. First a calibration step is performed to equalise the signals in the front and in the back sections, secondly the L-correction is evaluated to compare the reconstructed COG coordinates with the true ones on the same z plane, and lastly the barycentre of the shower is corrected for its non-linear transversal profile.

The only filters applied to the MC simulation outputs were on the total energy deposited in the front and back section, expressed in number of photo-electrons produced, and on the x and y position to select only the central cell of the prototype.
Thanks to the GenerateParticleSource (GPS) function of GEANT4, it is possible to set the information about the particle source, as the energy, the position, the direction and the geometry of the beam. As a consequence, the beam was chosen to have a square dimension of a certain energy, therefore no filters were needed to correct for its angular distribution. In addition, the DWCs were not reproduced in the simulations. Then, also the filters on the correlation between their coordinates described in Section 3.2 were not considered.

4.1.1 Calibration Procedure

Since the front and the back sections of each prototype differs in length, there is a different amount of energy deposited in each section. To correct for this effect and equalise the signals, a calibration procedure is needed. The *calibration factors* for the relative section are expressed in Equation 4.1,

$$c_{back} = \frac{NPE_{back}}{E_{back}} \qquad c_{front} = \frac{NPE_{front}}{E_{front}} \tag{4.1}$$

where NPE_{front} and NPE_{back} represent the number of photo-electrons produced in the prototype after the interaction between the beam particles and the active part of the module, and E_{front}, E_{back} correspond to the energy deposited into the scintillating fibres in the front and in the back section respectively.
To equalise the output signal coming from the front and the back sections, the distribution 4.1 is plotted as a function of the beam energy. The ratio between the calibration factors gives the correction to apply to the signals. For instance, in this case the calibration factor for the front section was set to 1, and the one for the back is obtained from the mean of that distribution (an example is shown in Figure 4.3).

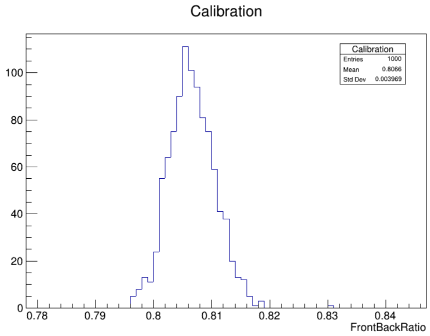

Figure 4.3: Example of the distribution of the calibration factor for the back section, keeping the front factor equals to 1.

The calibration factor for the back section is then plotted as a function of the beam energy in Figure 4.4. It is possible to notice that for the SpaCal W prototype it follows a decreasing trend at low energies and then it reaches a constant term above 20 GeV. For the SpaCal Pb instead it is evident that the same quantity is approximately constant around the same value when the energy changes.

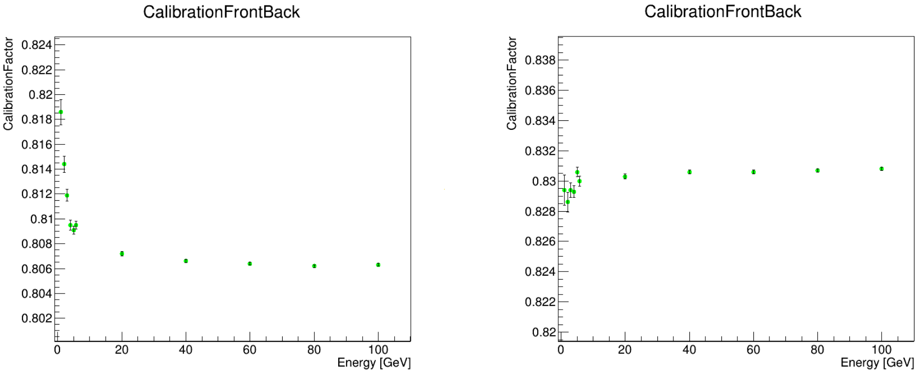

(a)

(b)

Figure 4.4: Calibration factor for the back section as a function of the beam energy for the SpaCal W (left) and SpaCal Pb (right) prototypes.

The behaviour described in Figure 4.4 could be associated to the different sampling fraction of the two prototypes leading to a different shower development within the detector.
Afterwards, once the calibration factors are extrapolated from the previous plots, the signals of the front and the back section can be equalised by dividing the photo-electrons output by the corresponding calibration factor.

4.1.2 L-function Parameters

The L-function is needed to correct the COG coordinates for the longitudinal shower development within the detector. The first step is to extrapolate the p_0 and p_1 parameters of the Equation 1.11 from MC simulations through the information on the initial direction of the particle given by the momentum (p_x, p_y, p_z) and the position of the source corresponding to the vertex (x_v, y_v, z_v).
The longitudinal centre of gravity of the shower z_{cog} for the front and the back sections is obtained from the previous quantities and from the transversal barycenter (x_{cog}, y_{cog}) evaluated with Equation 3.1. Then it is plotted as a function of the logarithm of the beam energy and p_0 and p_1 correspond to the linear fit parameters.

This procedure is applied both to the SpaCal W and the SpaCal Pb prototypes. Once p_0 and p_1 are known, it is possible to evaluate the longitudinal centre of gravity of the shower for a given energy through the Equation 1.11 also for the test-beam data.

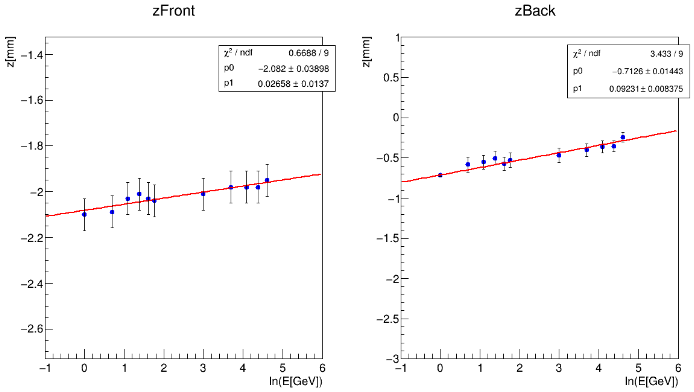

Figure 4.5: Longitudinal centre of gravity of the shower in the front (left) and back (right) section as a function of the logarithm of the beam energy for the SpaCal W prototype.

4.1.3 S-function Parameters

In order to obtain the spatial resolution, as explained in Section 3.2, the COG coordinates need to be corrected for the non-linear transversal profile of the shower using the S-function expressed in Equation 1.12. The first step is then to run a set of MC simulations with a large beam ($20 \times 20mm^2$), such that it covers a big portion of the SpaCal Pb cell and the entire central cell for the SpaCal W. This procedure is applied for different beam energies to check whether they follow an energy-dependent trend.

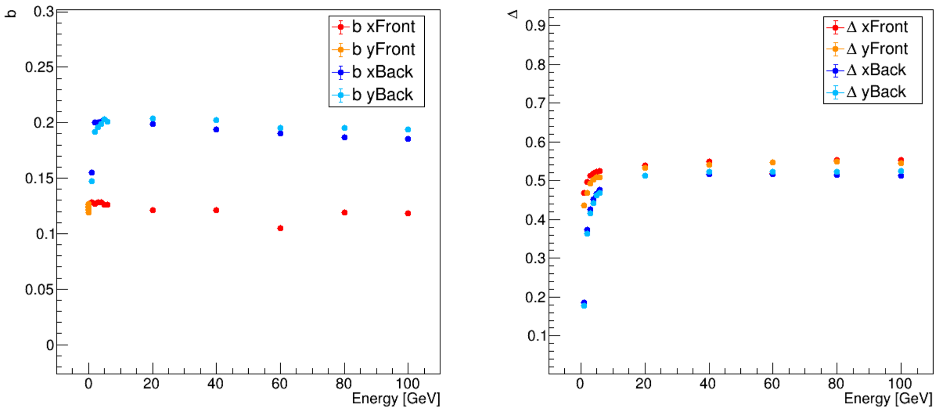

Figure 4.6: Plots of the trend that the b and Δ parameter of the S-function follows when the beam energy changes, considering the front and the back sections separately.

An observation from the plots in Figure 4.6 is that the parameters of the S-function are not constant, but vary with energy. This behaviour could be associated with the fact that the prototype reproduced is rotated of 3°+3°. Therefore the dependence of the

barycentre of the electromagnetic shower from the beam energy plays a non-negligible role.
Also, when the beam energy increases, the electromagnetic shower goes deeper in the prototype and the energy sharing changes. For this reason a low-energy electron will deposit most of its energy in the front, where it spreads out transversely. On the contrary, a very energetic electron will produce a narrow shower in the front, which widens more in the back. The energy dependence of the S-function parameters is then justified, since they are related to the width the shower.
In our case, the b and Δ parameters, that will be used to correct the COG, were calibrated with the large beam.

The second step is to run another set of MC simulation with a square narrow beam, of dimension $1.7 \times 1.7mm^2$, such that only a small portion of the central cell of the prototype is hit by particles. The datasets with the narrow beam are used to estimate the spatial resolution of the prototype.

4.2 Monte Carlo Simulations Results

As mentioned in the previous section, a first set of MC simulation with a large beam $20 \times 20mm^2$ is used to calibrate the parameters of the S-function. These in turn will be fundamental to correct the centre of gravity coordinates evaluated with the $1.7 \times 1.7mm^2$ narrow beam for the transversal profile of the electromagnetic shower.

4.2.1 Spatial Resolution Results

The spatial resolution was studied as a function of the beam energy only with a module inclination of $3°+3°$ for the front and the back sections separately and then combined. Both the standard and the weighted average appear to provide approximately the same results at low energies and when the spatial resolution is almost equal in the two sections. Then the choice of the weighted mean average over the standard one is dictated by the fact that it takes into account that the spatial resolution improves in the back at higher energies compared to the front section. This is because the shower develops mostly in the back, where more energy deposition takes place. Therefore, when this occurs the weighted mean method gives better results than the standard one, as shown in Figure 4.7. However, the standard average is still useful since in the calorimeter it will not be easy to know with which weights to combine the information, event by event.

At a later stage, the spatial resolution was also investigated changing the position of a square portion of the beam within the central cell.

SpaCal W The first step involves the study of the spatial resolution as a function of the beam energy shooting in the centre of the cell, in the range between 1 GeV and 100 GeV with the front and the back considered as independent in Figure 4.8 and combined in Figure 4.9.

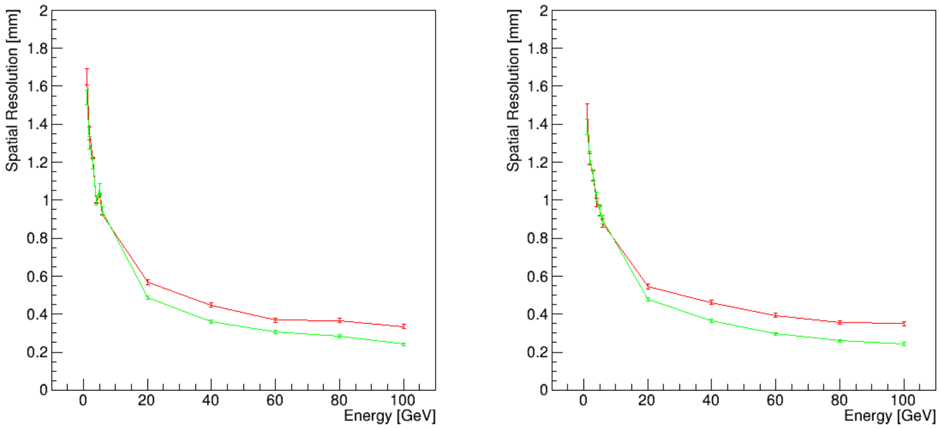

Figure 4.7: Standard mean (red) vs weighted mean (green) method for the front and back combined spatial resolution along x direction (left) and y direction (right). Results obtained from MC simulation for the SpaCal W prototype.

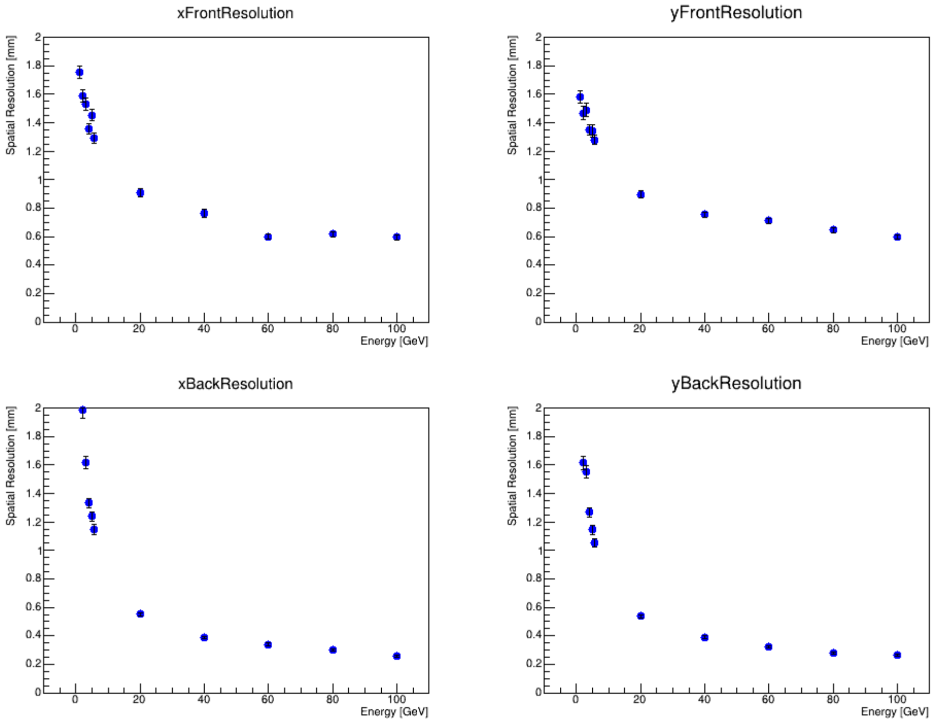

Figure 4.8: Spatial resolution as a function of the beam energy for SpaCal W considering front and back sections separately. MC simulations with the prototype rotated of 3°+3°.

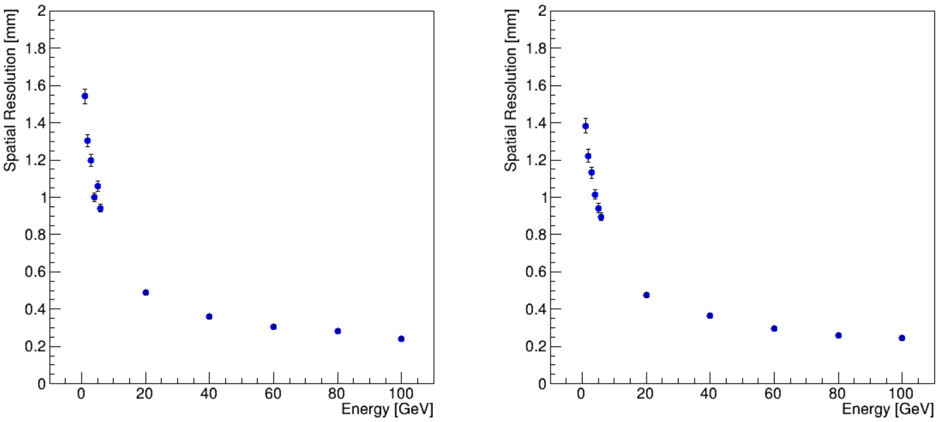

Figure 4.9: Spatial resolution as a function of the beam energy for SpaCal W considering front and back sections combined with the weighted mean method along x (left) and y (right) direction. MC simulations with the prototype rotated of 3°+3°.

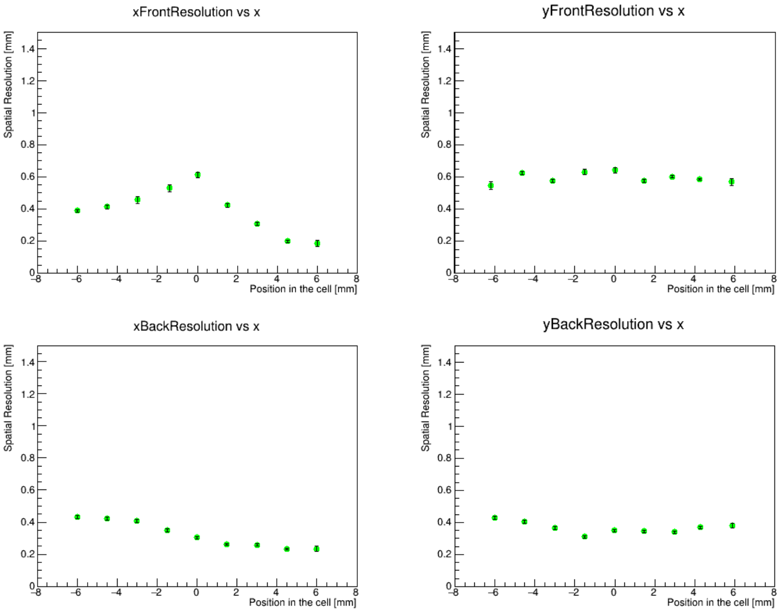

Figure 4.10: Spatial resolution as a function of the position in the cell, moving the $1.5 \times 1.5mm^2$ beam with 80 GeV energy along x for SpaCal W. MC simulations with the prototype rotated of 3°+3°.

The position resolution meets the expectations, improving as the beam energy increases. In particular the function is steeper for low energies, while above 20 GeV it tends to be less energy-dependent. The spatial resolution seems to follow the same trend

as the energy resolution, reflecting its dependence on the energy measurement. This quantity in fact is obtained with a better precision when it reaches higher values.
Moreover, the spatial resolution was investigated also for several position within the central cell of the prototype. A square portion of the beam, with $1.5 \times 1.5mm^2$ dimension was moved along x while keeping the y coordinate fixed, then along y keeping x set to 0, and finally along the diagonal.

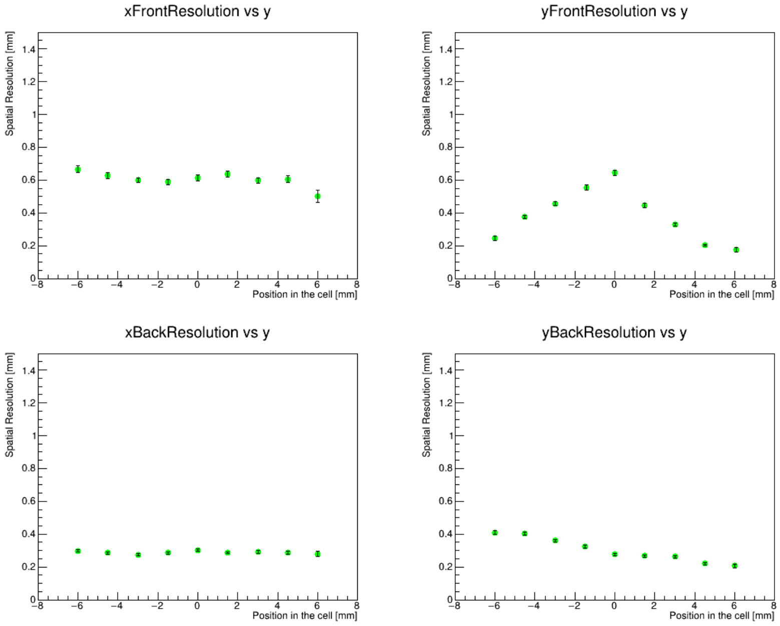

Figure 4.11: Spatial resolution as a function of the position in the cell, moving the $1.5 \times 1.5mm^2$ beam with 80 GeV energy along y for SpaCal W. MC simulations with the prototype rotated of 3°+3°.

From the Figure 4.11 it can be noticed that along the direction where the beam is moved the spatial resolution seems to be worse in the very centre of the cell, while along the other axis it maintains a constant trend. In addition, moving along the diagonal a maximum in the position resolution which corresponds to the centre of the cell in the front can be observed, while for the back section an asymmetry in the distribution with a peak shifted with respect to the centre is observed because the module is rotated of 3°+3°.
A possible explanation to this effect lies in the fact that the centre of gravity of the cluster strongly depends on the energy sharing between the cells. Therefore, the spatial resolution is expected to be better when the energy is shared over as many cells as possible, so that the centre of gravity can be calculated more accurately.

SpaCal Pb In the same way it was done for the SpaCal W prototype, first the spatial resolution was investigated as a function of the beam energy, in the range between 1

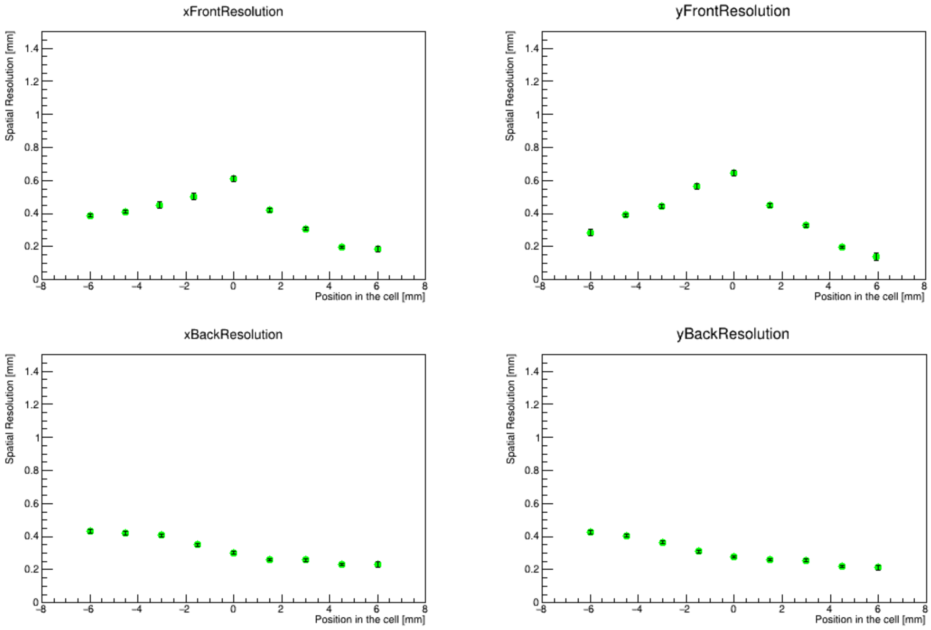

Figure 4.12: Spatial resolution as a function of the position in the cell, moving the $1.5 \times 1.5 mm^2$ beam with 80 GeV energy along the diagonal for SpaCal W. For example a position equals to 3 mm means $(x, y) = (3mm, 3mm)$. MC simulations with the prototype rotated of 3°+3°.

GeV and 100 GeV with the front and the back considered separately in Figure 4.13 and combined in Figure 4.14.

As it has already been observed, the position resolution improves when the front and the back sections are combined and it tends to get better as the beam energy increases.

Moreover, the spatial resolution was investigated also as a function of the position within the central cell of the prototype. A square portion of the beam, with $3 \times 3mm^2$ dimension was moved along x while keeping the y coordinate fixed, then along y keeping x set to 0, and finally along the diagonal.

From the Figure 5.4 it can be noticed that along the direction where the beam is moved the spatial resolution seems to be slightly worse in the very centre of the cell, but anyway almost compatible with a constant trend. Instead along the axis which is kept fixed, the spatial resolution maintains a constant trend. In addition, moving along the diagonal the position resolution reaches its worse value at the centre of the cell in the front, while for the back section it is shifted with respect to the centre because the module is rotated of 3°+3°. However the peak that represent the maximum is not so evident: the trend could be approximately described by a flat function.

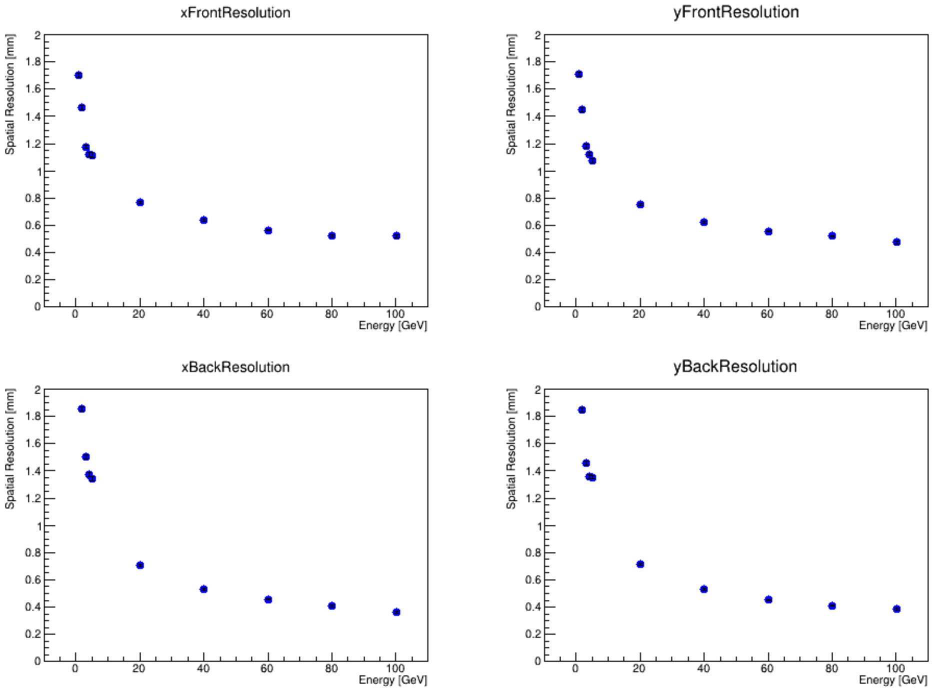

Figure 4.13: Spatial resolution as a function of the beam energy for SpaCal Pb considering front and back sections separately. MC simulations with the prototype rotated of 3°+3°.

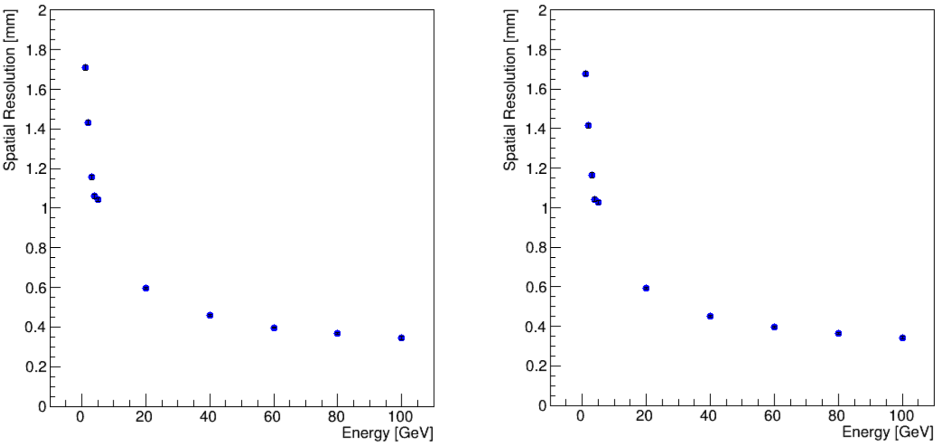

Figure 4.14: Spatial resolution as a function of the beam energy for SpaCal Pb considering front and back sections combined with the weighted mean method along x (left) and y (right) direction. MC simulations with the prototype rotated of 3°+3°.

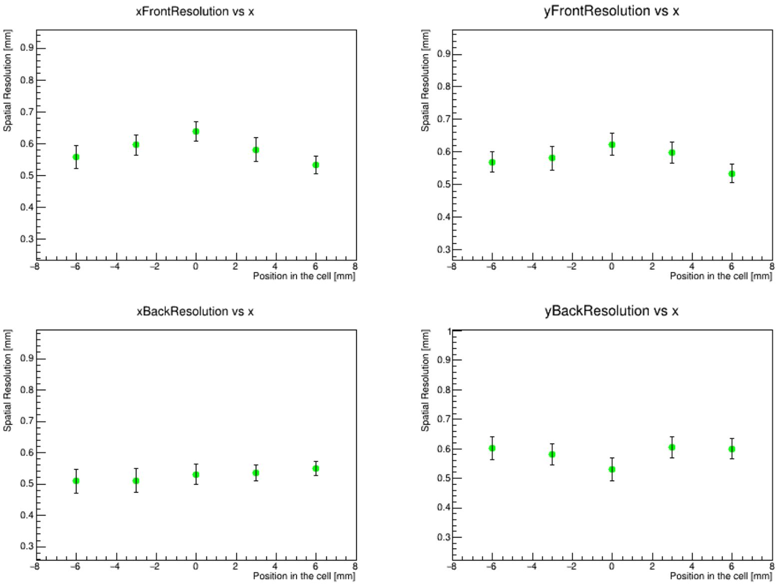

Figure 4.15: Spatial resolution as a function of the position in the cell, moving the $3 \times 3mm^2$ beam with 40 GeV energy along x for SpaCal Pb. MC simulations with the prototype rotated of 3°+3°.

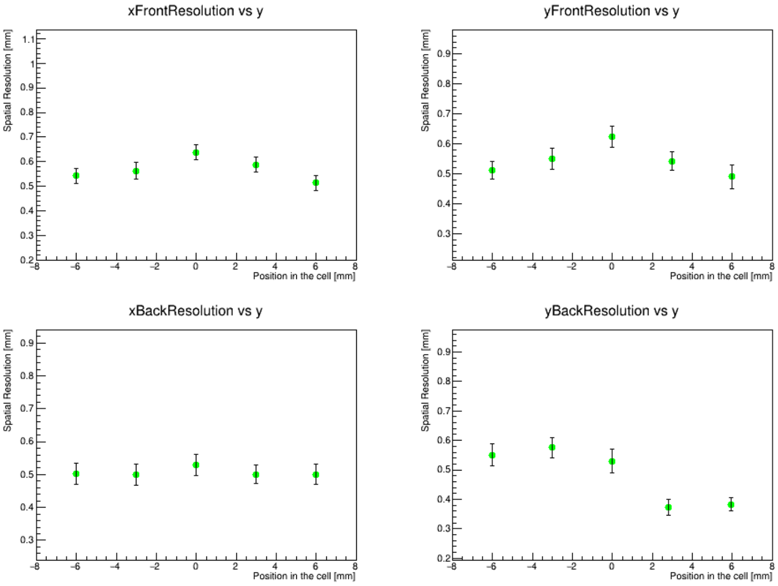

Figure 4.16: Spatial resolution as a function of the position in the cell, moving the $3 \times 3mm^2$ beam with 40 GeV energy along y for SpaCal Pb. MC simulations with the prototype rotated of 3°+3°.

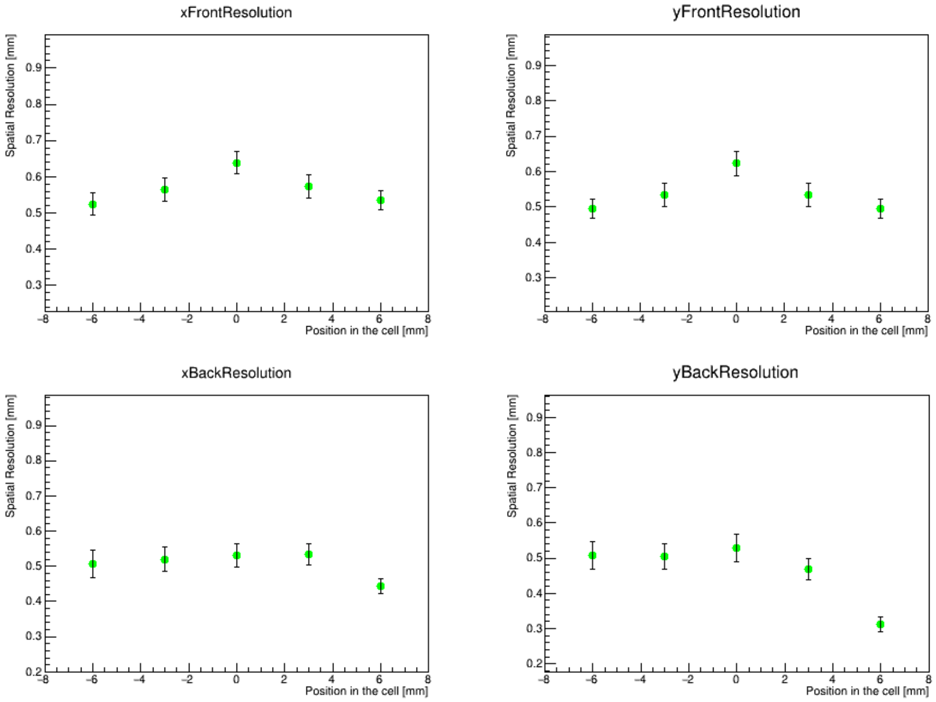

Figure 4.17: Spatial resolution as a function of the position in the cell, moving the $3 \times 3mm^2$ beam with 40 GeV energy along the diagonal for SpaCal Pb. For example a position equals to 3 mm means $(x, y) = (3mm, 3mm)$. MC simulations with the prototype rotated of 3°+3°.

Chapter 5

Test Beam studies with SpaCal Prototypes for ECAL

The two SpaCal prototypes described in the previous chapter were tested at SPS [18] and DESY facilities with an electron beam of energy between 1GeV/c^2 and 100GeV/c^2 in total.
It was possible not only to choose the energy of the beam (for simplicity it will be expressed in $c = 1$ units), but also to vary the beam dimension along the horizontal (x-axis) and the vertical (y-axis) directions. At SPS the beam width was tuned changing the currents of the quadrupoles, instead at DESY different collimators were available.

5.1 Calibration Procedure

During the Beam Test that took place in November at H4 (SPS) and in May at DESY, each longitudinal section of the prototypes was divided in nine cells, forming a 3×3 cluster, and connected to a PMT in different ways to test the better configuration, as described in Section 2.3.3. In particular, among the light transports tested there were light guides, several optical couplings, and a fibres bundle for the central cell of the front section of the SpaCal Pb module.
For the energy measurements, the aim was to obtain the total energy E_T deposited in the calorimeter module by an incoming particle, starting from the individual energies deposited in each cell E_i.

$$E_T = \sum_{i=1}^{18} E_i \tag{5.1}$$

What is actually obtained is a pulse shape V(t), which is first integrated over a 400 ns gate, and then divided by the load resistence of 50Ω to get the total charge collected on the anode. If we consider that the module is split longitudinally in front and back section, at the end the output consists of 18 integrated charge signals Q_i.

Afterwards a calibration procedure [17] is performed in order to convert the PMTs

charge output into deposited energy for each cell and to equalise the output signal coming from the same beam particle in the front and in the back section. The proportionality coefficient between these two quantities, the *calibration factor*, allows to obtain the total energy deposited by an incoming particle event by event and to compensate the gain, light collection efficiency and quantum efficiency variations between different cells.
First, the front PMTs' bias voltages were tuned to achieve the same peak position of the charge histograms of each cell with the electron beam hitting the centre of that cell. Afterwards, the front section was removed and the same procedure was repeated for the back section. Then, by selecting only events hitting in a 20×20 mm^2 square for SpaCal W and 40×40 mm^2 for SpaCal Pb in the centre of the back section, a set of 9 calibration coefficients c_j for the back cells was found by minimising the residuals.

$$\sum_{i_{ev}=1}^{N_{ev}} \left[E_{beam} - \sum_{j=1}^{9} c_{b,j} S_{b,j} \right]^2 = \min, \tag{5.2}$$

where $S_{b,j}$ and $c_{b,j}$ are the integrated charge, E_{beam} equals to 3 GeV at DESY and 40 GeV at SPS and the calibration coefficient of the j-th cell in the back section, and i_{ev} the i-th event of the dataset. Afterwards, the front section was reinstalled, and the procedure was repeated for the whole module keeping the calibration coefficients of the back constant:

$$\sum_{i_{ev}=1}^{N_{ev}} \left[E_{beam} - \sum_{j=1}^{9} (c_{f,j} S_{f,j} + c_{b,j} S_{b,j}) \right]^2 = \min, \tag{5.3}$$

where $S_{f,j}$ and $c_{f,j}$ are the integrated charge and the calibration coefficient of the j-th cell in the front section.

5.2 Test Beam Results

Datasets with different energies were acquired during the beam tests in at SPS and at DESY facilities, in the range between 20-100 GeV with 20 GeV interval and 1-5 GeV with 1 GeV interval respectively. Also the inclination of the prototypes was changed throughout the runs.

5.2.1 Spatial Resolution Results

The spatial resolution was first investigated as a function of the beam energy and for different incident angles of the particle for both the SpaCal W and SpaCal Pb prototypes. Furthermore a scan of the spatial resolution for different x and y positions along the horizontal and the vertical axis, and along one the diagonals within the module was performed. For these measurements the PMTs involved in the double electronic readout of the signals were the Hamamatsu R7899-20 and R11187 for the SpaCal Pb, while the R12421 for the SpaCal W (see Section 2.3.3).

SpaCal W The first measurement performed is the energy scan for different module inclinations. More in details datasets were acquired for 1, 2, 3, 4, 5, 20, 40, 60, 80 and 100 GeV particle energies to investigate the dipendence of the spatial resolution from the energy of the electron/positron beam, considering front and back separately and then combined with the weighted mean expressed in Equation 3.4.

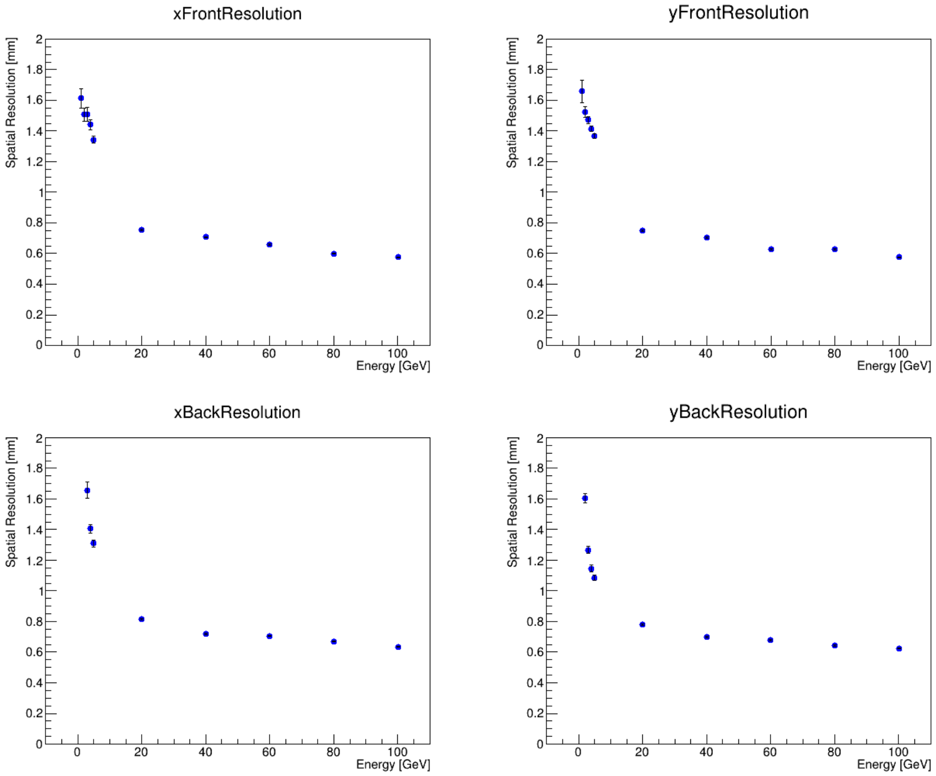

Figure 5.1: Spatial resolution as a function of the beam energy for SpaCal W considering front and back sections separately. Dataset with the prototype rotated of 3°+3°.

In the plot shown in Figure 5.1 it is possible to notice that the position resolution of the beam particles improves when their energy increases and with the same trend for the front and the back section. In particular, both parts of the prototype presents approximately the same performance in terms of spatial resolution for a given beam energy above 20 GeV, reaching values below 1 mm.

After this step, the front and back section were combined using the weighted mean method.

As for the front and back separated, in Figure 5.2 it is clear that the position resolution is always $< 1mm$ for the beam energies tested above 20 GeV, and the module achieves better performance when the energy increases.

Afterwards a spatial resolution scan was also performed as a function of the position within the central cell. In order to do that, a square region of the beam with $1.5 \times 1.5mm^2$

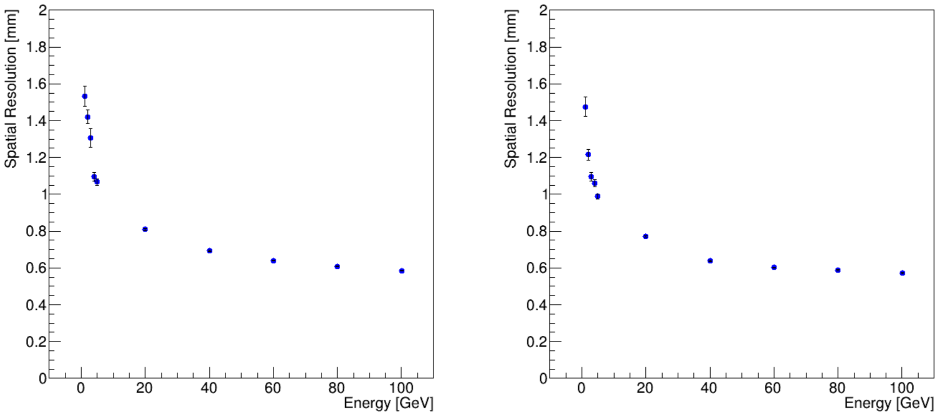

Figure 5.2: Spatial resolution as a function of the beam energy for SpaCal W considering front and back sections combined with the weighted mean method, along x (left) and y (right) direction. Dataset with the prototype rotated of 3°+3°.

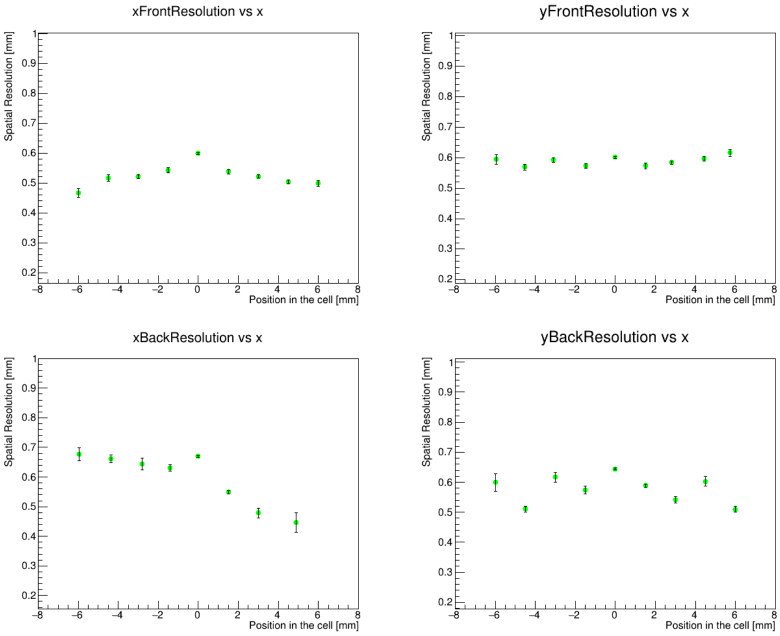

Figure 5.3: Spatial resolution as a function of the position in the cell, moving the $1.5 \times 1.5 mm^2$ beam with 80 GeV energy along along x for SpaCal W. Dataset with the prototype rotated of 3°+3°.

dimension was selected and moved first along the x axis keeping the y coordinate fixed, then the same procedure was applied to the y direction. In addition the beam was used

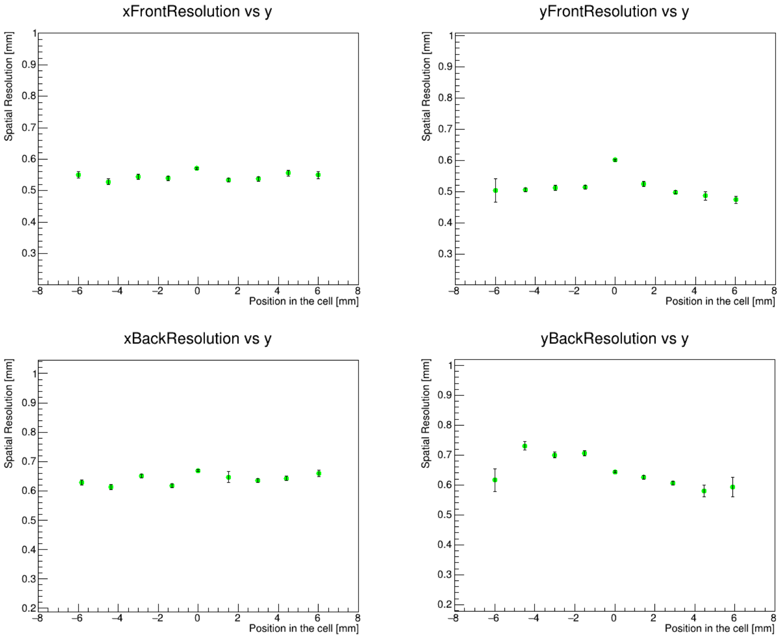

Figure 5.4: Spatial resolution as a function of the position in the cell, moving the $1.5 \times 1.5mm^2$ beam with 80 GeV energy along along y for SpaCal W. Dataset with the prototype rotated of 3°+3°.

to scan also the cell along the diagonal in terms of position resolution.
From the Figure 5.4 it can be noticed that along the direction where the beam is moved the spatial resolution seems to be worse around 0, i.e. in the centre of the cell. Along the other axis it maintains approximately a constant trend. Moreover, moving along the diagonal (in Figure 5.5) a maximum in the position resolution plot is observed for both x and y directions, which in the front corresponds to the centre of the cell. On the other hand, in the back section the worse performance is associated to a shifted position with respect to the centre because the module is tilted of 3°+3°.
When the beam hits the centre, depending on the Molière radius, the shower is more transversally contained within the cell. Otherwise, when the particles are shot near the borders, part of the electromagnetic shower hits the adjacent cell too. Therefore, this configuration leads to a more precise reconstruction of the barycentre of the cluster.

Since different datasets for several rotation angles were acquired in the energy range between 20 and 100 GeV, a summary plot for the SpaCal W is shown in Figure 5.6, where the spatial resolution is expressed as a function of the beam energy for different angles of inclination of the prototype.

From the picture some observations can be done: the spatial resolution of the front and the back section combined tends to follow the same decreasing trend as the beam energy increase for all the rotation angles tested. In particular, the smaller is the angle,

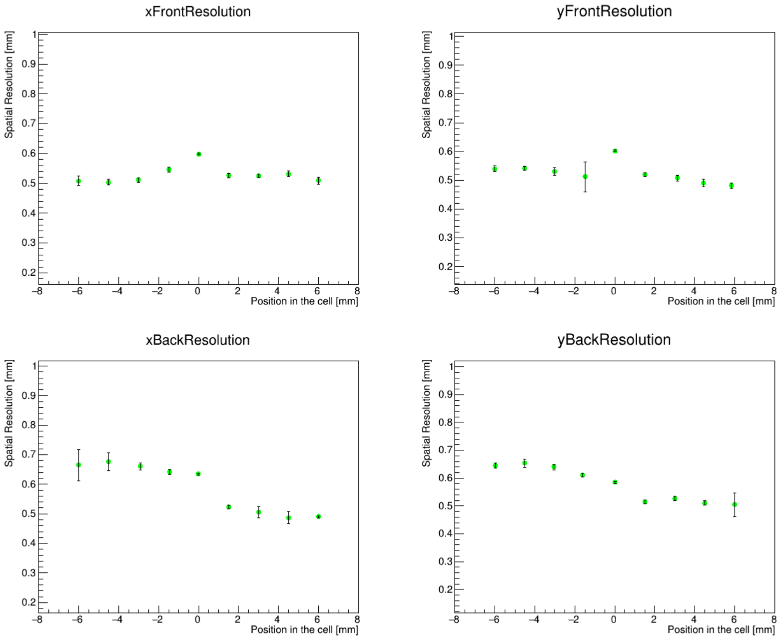

Figure 5.5: Spatial resolution as a function of the position in the cell, moving the $1.5 \times 1.5mm^2$ beam with 80 GeV energy along the diagonal for SpaCal W. Dataset with the prototype rotated of 3°+3°.

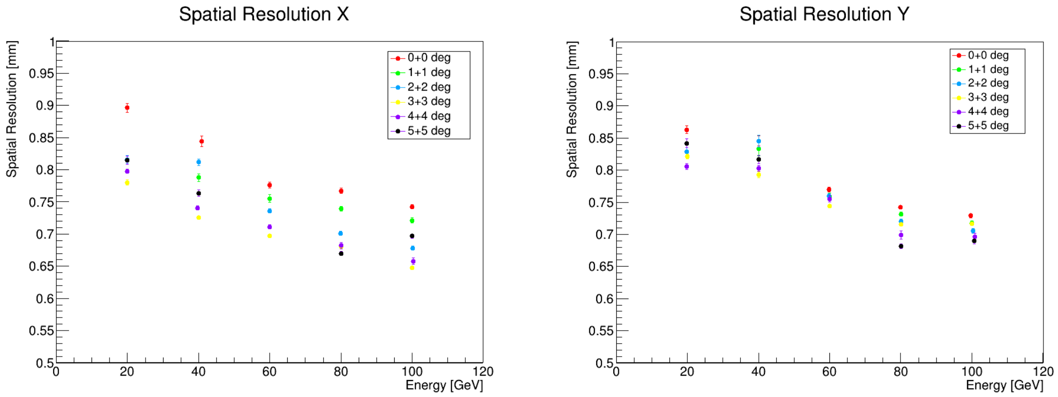

Figure 5.6: Spatial resolution of the front and back section combined with the weighted mean method, as a function of the beam energy and for several rotation angles of the prototype SpaCal W.

the worse is the spatial resolution. The position ability of the SpaCal W reaches an optimal value when the prototype is rotated by 3-4°

SpaCal Pb Similarly a scan of the position resolution for different beam energies, that are the same used for the SpaCal W (except for 100 GeV), was performed. Considering first front and back separately it is possible to observe the same decreasing trend, shown in Figure 5.7, in spatial resolution as a function of beam energy that was previously observed for the other prototype.

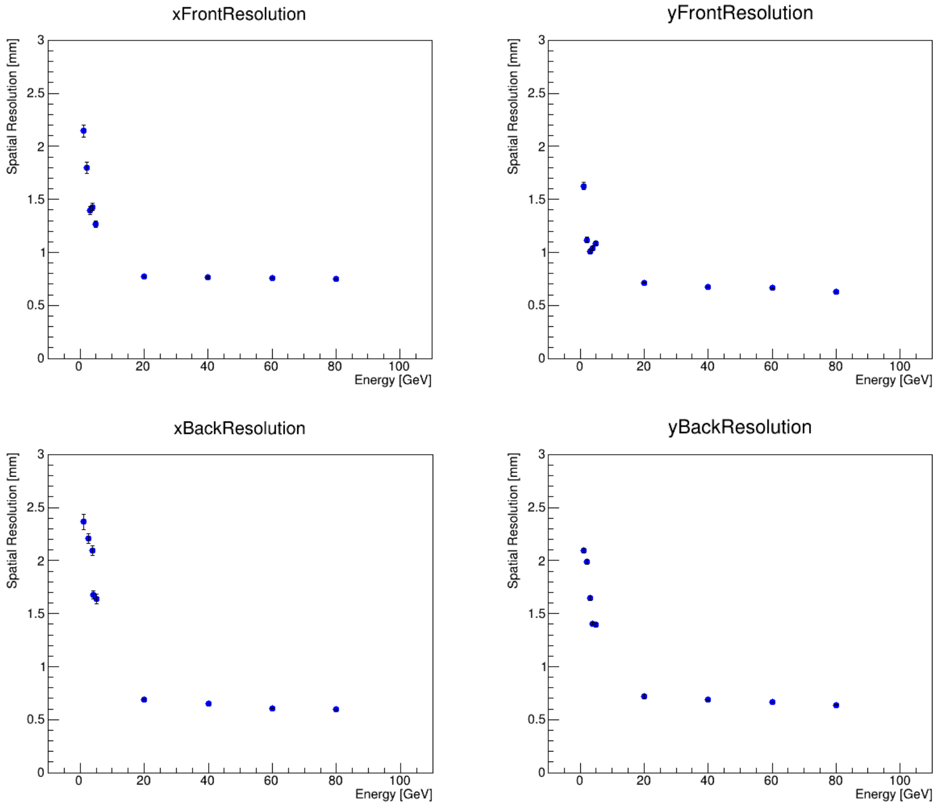

Figure 5.7: Spatial resolution as a function of the beam energy for SpaCal Pb considering front and back sections separately. Dataset with the prototype rotated of 3°+3°.

The spatial resolution is investigated also for the front and back sections combined with the weighted average expressed in Equation 3.4. For the datasets with a rotation angle of the prototype equals to 3°, both sections, if considered as indipendent, present a similar spatial resolution above 20 GeV, which is below 1 mm. For lower energies instead the back section has a worse performance, reaching values above 2 mm. This behaviour is justified by the fact that the electromagnetic shower develops mainly in the front at low energies, and consequently the energy measurement that enters in the spatial resolution evaluation in the back is exposed to greater fluctuations. Additionally, the combination of the two sections with the weighted mean method brings slightly better results in terms of position resolution than when they are considered separately, achieving the performance required for the upgrade.

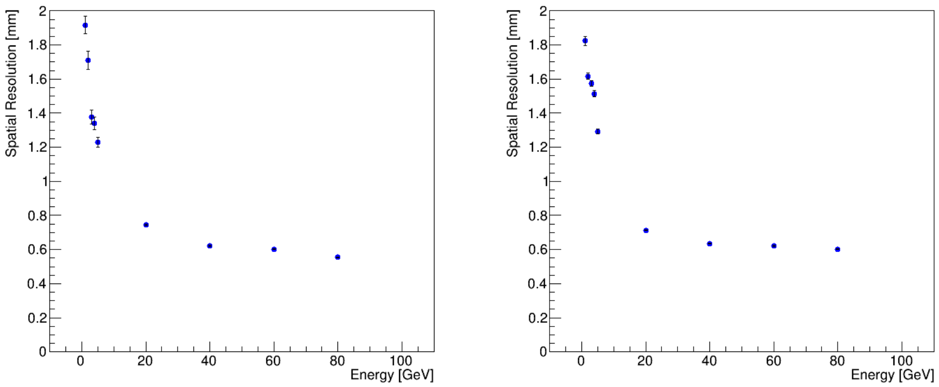

Figure 5.8: Spatial resolution as a function of the beam energy for SpaCal Pb considering front and back sections combined with the weighted mean method along x (left) and y (right) direction. Dataset with the prototype rotated of 3°+3°.

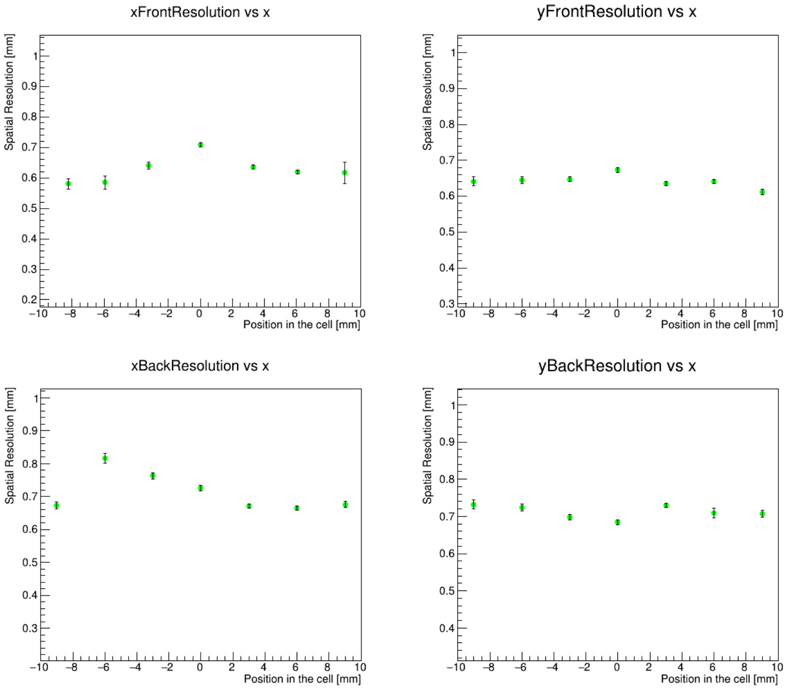

Figure 5.9: Spatial resolution as a function of the position in the cell, moving the $3\times 3mm^2$ beam with 40 GeV energy along x for SpaCal Pb. Dataset with the prototype rotated of 3°+3°.

Afterwards a spatial resolution scan was also performed as a function of the position within the central cell by selecting a square region of the beam of $3 \times 3mm^2$. As for the

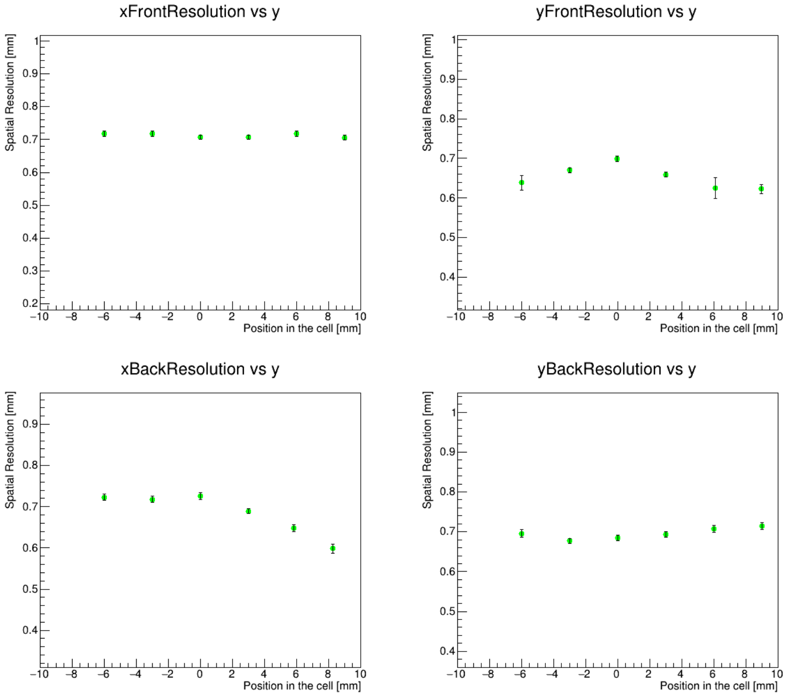

Figure 5.10: Spatial resolution as a function of the position in the cell, moving the $3 \times 3mm^2$ beam with 40 GeV energy along y for SpaCal Pb. Dataset with the prototype rotated of 3°+3°.

SpaCal W, the beam was moved first along the x axis keeping the y coordinate fixed, then along y keeping the x coordinate fixed, and at the end along the diagonal.

In this case, the trend of the spatial resolution moving along the diagonal in Figure 5.11 is not as evident as for the other prototype. One can conclude that the resolution of the position of the particle is slightly worse in correspondence of the centre of the cell at least along the x direction in the front section, while for the back the maximum is shifted around (-4, -4) due to the rotation of the prototype. However, on y direction the position resolution behaves as a constant function within the uncertainties for both sections.

From these results one can deduce that the geometry of the SpaCal Pb prototype, in terms of the Molière radius of its cells, is optimised for the spatial resolution. Conversely, the SpaCal W prototype design could still be improved: in practice, the current dimension of the cells leads to a worse energy sharing with the adjacent ones. In other words, the optimal cell size would be smaller than $15{\times}15mm^2$.

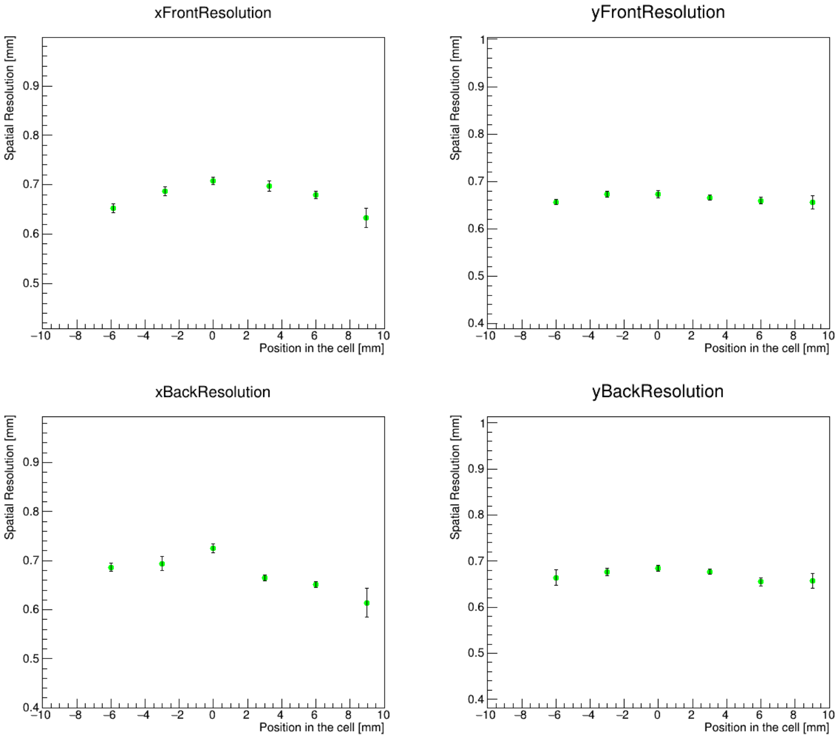

Figure 5.11: Spatial resolution as a function of the position in the cell, moving the $3 \times 3mm^2$ beam with 40 GeV energy along the diagonal for SpaCal Pb. Dataset with the prototype rotated of 3°+3°.

5.2.2 Angular Resolution Results

The first step was to check the relation between the angle of incidence of the particle on the front surface, evaluated using the expression 3.5, with the nominal angle of rotation of the prototype θ_0, which was the one set in the configuration file during the data acquisition. To understand whether the angle of inclination of the particles actually corresponds to the set angle of rotation, the relation between these quantities should be described by a linear function.

That is the case for the SpaCal W, but since the slope is not equal to 1, θ is compressed with respect to the nominal angle, leading to a better spatial resolution than the real one. In addition, it is possible to identify an offset that is related to the non-perfect alignment of the beam with the module. From the plot shown in Figure 5.12 one can notice that when the prototype is not rotated, the measured angle corresponds to a non-zero value, which in particular is equal to the fit parameter p_0. In the end, the linear relation is used to correct the angles bringing them back to their real values before evaluating the angular resolution.

After that, the angular resolution, obtained as explained in Section 3.3 was investigated

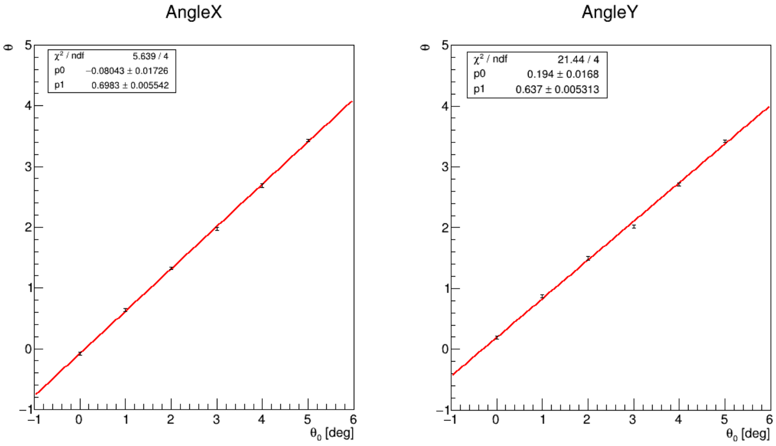

Figure 5.12: Relation between the θ angle of incidence of the particle and the nominal angle θ_0 of rotation of the SpaCal W prototype.

as a function of the rotation angle of the prototype for a given beam energy. Many datasets with different inclination angles are available for the SpaCal W prototype, while for the SpaCal Pb only a few angles were acquired.

SpaCal W This prototype was tested with different energies in the range 20 -100 GeV with several rotation angles between 0° and 5°. The angular resolution was investigated as a function of the incident angle θ for a given beam energy.

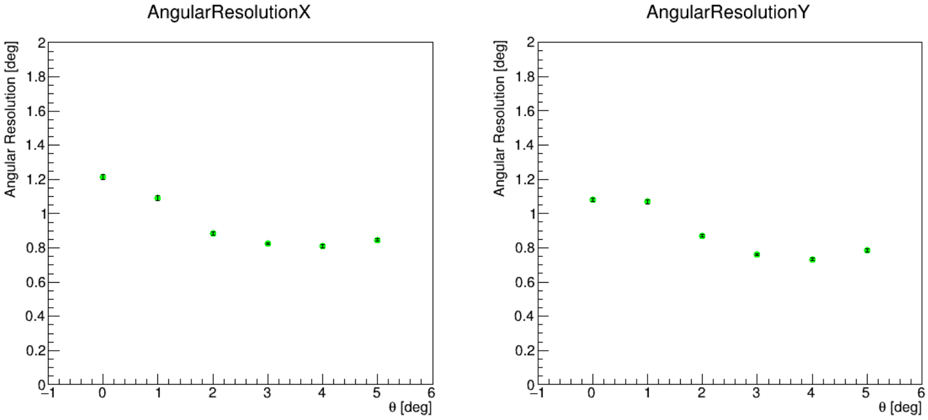

Figure 5.13: Angular resolution as a function of the incident angle θ of the particles for a 40GeV beam for SpaCal W.

An example is given in Figure 5.13, where it is possible to notice that the angular resolution seems to be worse when the rotation angle of the prototype is around 0°. Indeed the performance of the SpaCal worsen at small incident angles as a result of the fluctuations depending on whether the particle first enters into a fibre or the absorber.

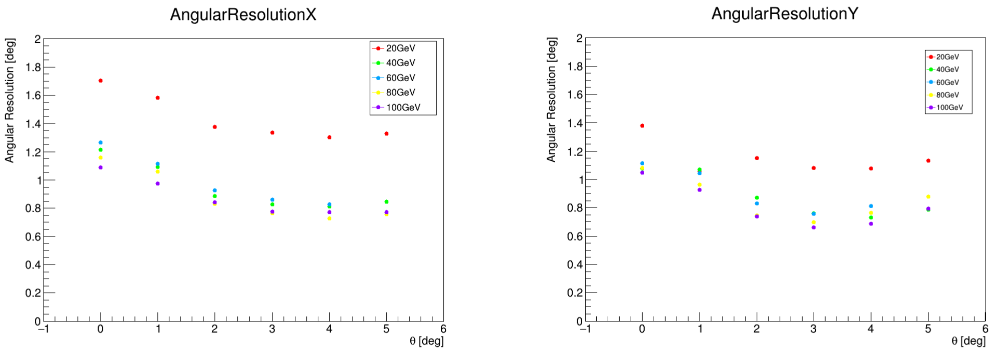

(a) (b)

Figure 5.14: Summarise plot of the angular resolution in degrees as a function of the incident angle θ for different beam energies for SpaCal W, along x (left) and y (right) directions.

After the study of the angular resolution for a given energy value it is possible to summarise the dependence of this quantity from the beam energy too, as shown in Figure 5.14.
In this case it is evident that the angular resolution is worse when the prototype is not rotated for all the energies tested, and it also has an energy dependence. Indeed when the beam energy increases the angular resolution improves in a similar way to the spatial resolution did. This can be explained by the fact that spatial and angular resolution are closely linked by the calculation of the centre of gravity coordinates, which in turns is based on the measurement of energy, and this measurement suffers from worse resolutions when the incidence angle is low.
Another observation is that, a part from the 20 GeV datasets, the angular resolution of the SpaCal W prototype lies around 1°.

SpaCal Pb This prototype was tested only with 40 GeV beam energy for different rotation angles, corresponding to 0°, 3° and 4°.

In Figure 5.15, one can notice that the angular resolution seems to be worse when the rotation angle is around 0°, as for the SpaCal W, due to the fluctuations depending on whether the particle first enters into a fibre or the absorber.

5.3 Conclusions

Some conclusions can be drawn from the comparison of the performance of the two promising technologies for the future upgrade of the electromagnetic calorimeter. Starting from the spatial resolution, the results considering the front and the back sections separately are shown in Figure 5.16 for the SpaCal W and the SpaCal Pb.

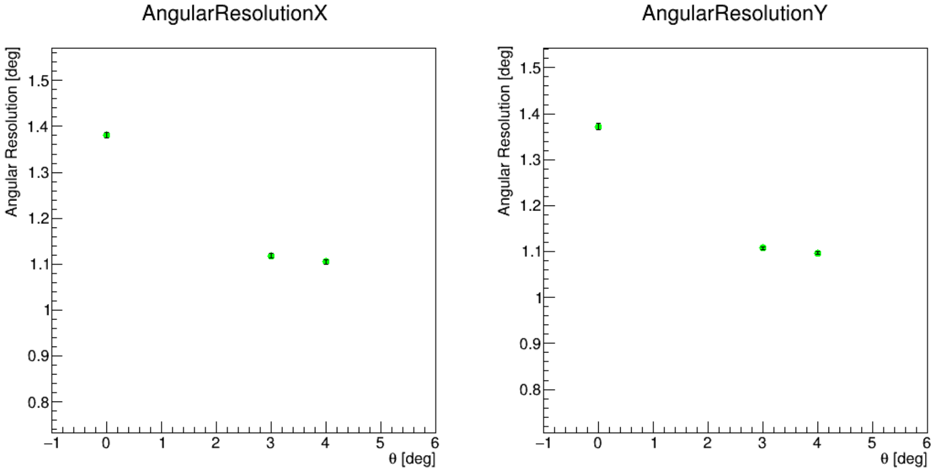

Figure 5.15: Angular resolution as a function of the incident angle θ of the particles for a 40GeV beam for the SpaCal Pb.

One point the two prototypes have in common is that the spatial resolution is worse in the front than in the back section for high beam energies. A possible explanation for this behaviour is associated with the different length of the two parts. Indeed the energy deposited in the active part of the detector is related proportionally to the length of the scintillating fibres, which is greater in the back than in the front section. In addition, since there is no preshower in the beam test configuration, the electromagnetic shower starts developing inside the front part of the prototype, leading to greater uncertainty due to fluctuations in its starting point.
On the contrary, for lower beam energies the back section has a worse position performance than the front. This is justified by the fact that the shower develops mainly at the beginning for low energy values, so there are greater fluctuations in the energy measurement in the back section.
Moreover, it is possible to get rid of the difference in the position resolution by considering the two sections no longer independent of each other, but combined with the weighted average method.
With this procedure, one can observe the overall spatial resolution along x and y direction.
From the comparison shown in Figure 5.17 it can be deduced that the spatial resolution improves as the beam energy increases, and that SpaCal W and SpaCal Pb results are compatible. More in details, above 20 GeV both the SpCal W and SpaCal Pb prototypes achieve the required 1 mm of overall spatial resolution, which is needed for the separation of the overlapping showers in the innermost part of the ECAL.

Furthermore, if one focuses on the angular resolution shown in Figure 5.18, it is evident that the SpaCal W prototype presents better results than the SpaCal Pb. Even if the angular resolution is strongly related to the position ability of the prototype, in the angle

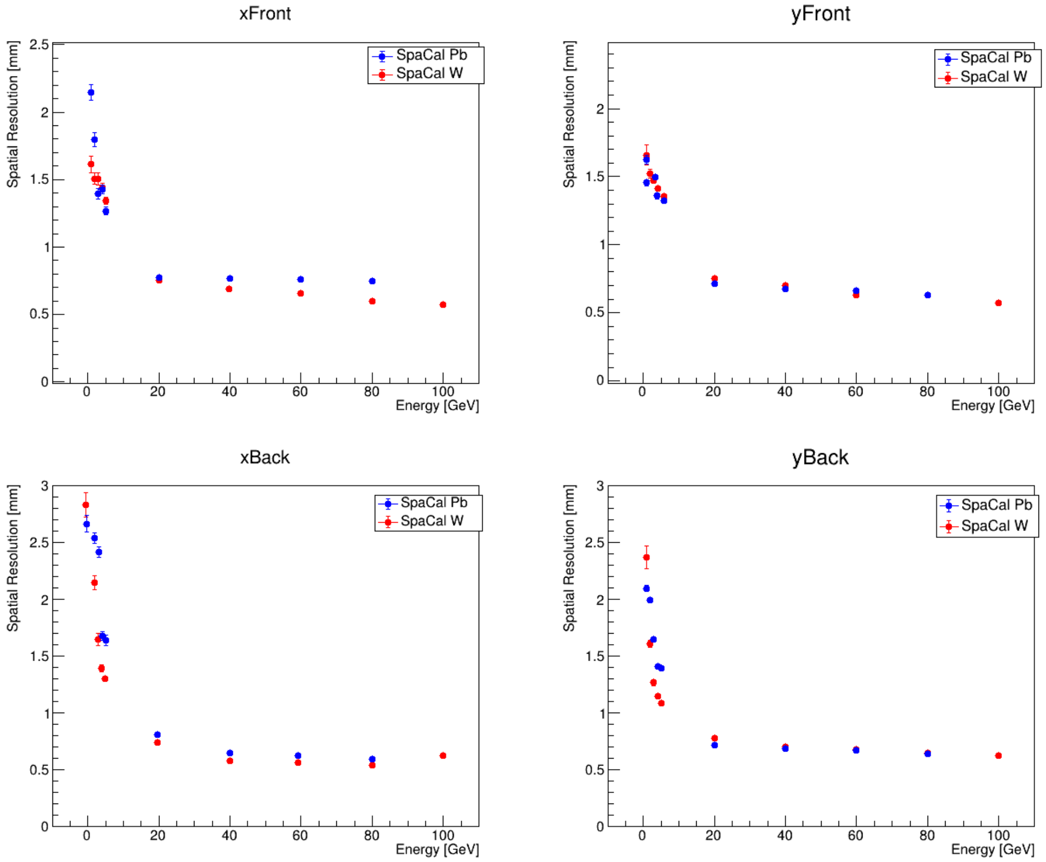

Figure 5.16: Spatial resolution as a function of the beam energy considering front and back sections separately, for the SpaCal W (red) and the SpaCal Pb (blue) rotated of 3° along the azimuthal and the altitude direction.

expression 3.5 includes an additional term, that comes from MC simulations, related to the mean of the barycentre of the energy deposition along z. The different spread of that distribution may be the cause of the discrepancy between the angular measurements of the two prototypes.

Moreover, the performances of the SpaCal prototypes worsen at small incident angles due to the fluctuations depending on whether the particle first enters into a fibre or the absorber.

Lastly, since the angular resolution depends on the rotation of the prototype, the optimal configuration forsees a rotation of the modules of 3° along the altitude and the azimuthal directions. With this setup it is possible to reach an angular resolution $\sim 0.8°$ for the SpaCal W and $\sim 1°$ for the SpaCal Pb.

Some observations can be done looking at the comparison between the outcomes of the MC simulations and the data acquired at SPS and DESY facilities, starting from the

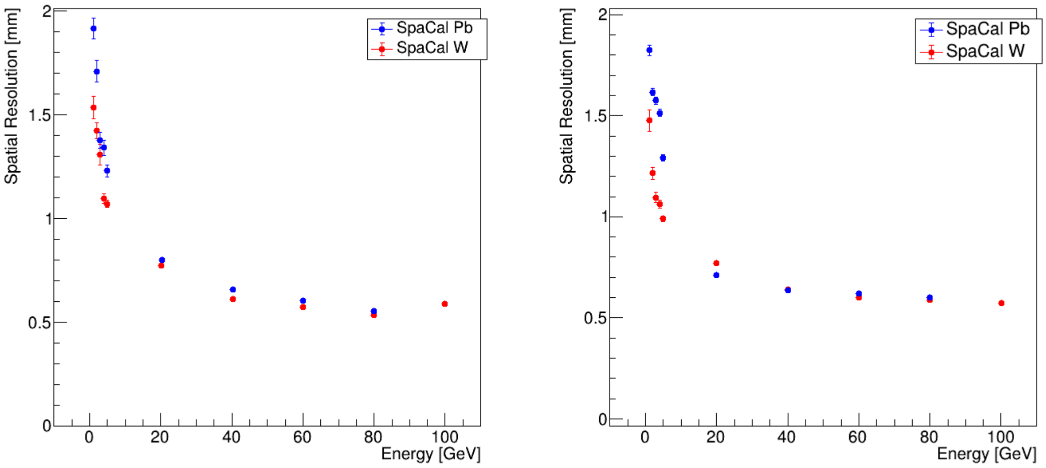

Figure 5.17: Spatial resolution as a function of the beam energy considering front and back sections combined with the weighted mean method along x (left) and y (right) direction, for the SpaCal W (red) and the SpaCal Pb (blue) rotated of 3° along the azimuthal and the altitude direction.

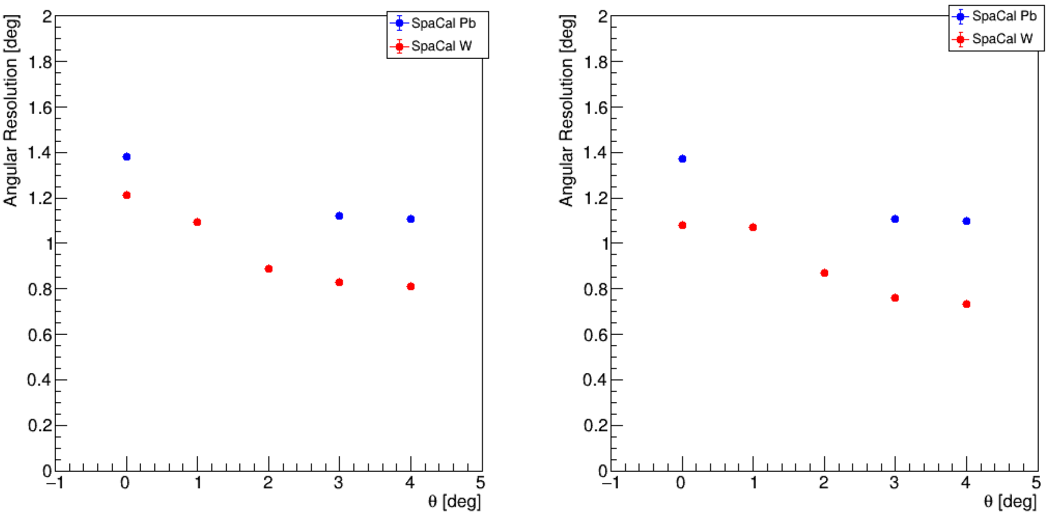

Figure 5.18: Angular resolution as a function of the rotation angle considering front and back sections combined with the weighted mean method along x (left) and y (right) direction, for the SpaCal W (red) and the SpaCal Pb (blue) for a 40 GeV beam energy.

spatial resolution with the front and the back sections considered separately and then combined.

In the first situation, it is possible to notice that the experimental results obtained with SpaCal Pb module are in agreement with the MC simulation outcomes for both sections. The data for the SpaCal W, instead, show that the the test-beam results match well the simulations in the front section, while the measurements for the back do not fit the expected values for the spatial resolution.
In addition, from the plots in Figure 5.19 and in Figure 5.20, one can notice that the spatial resolution seems to be slightly worse in the front section for lower energies also for MC simulations, confirming what has already been observed.

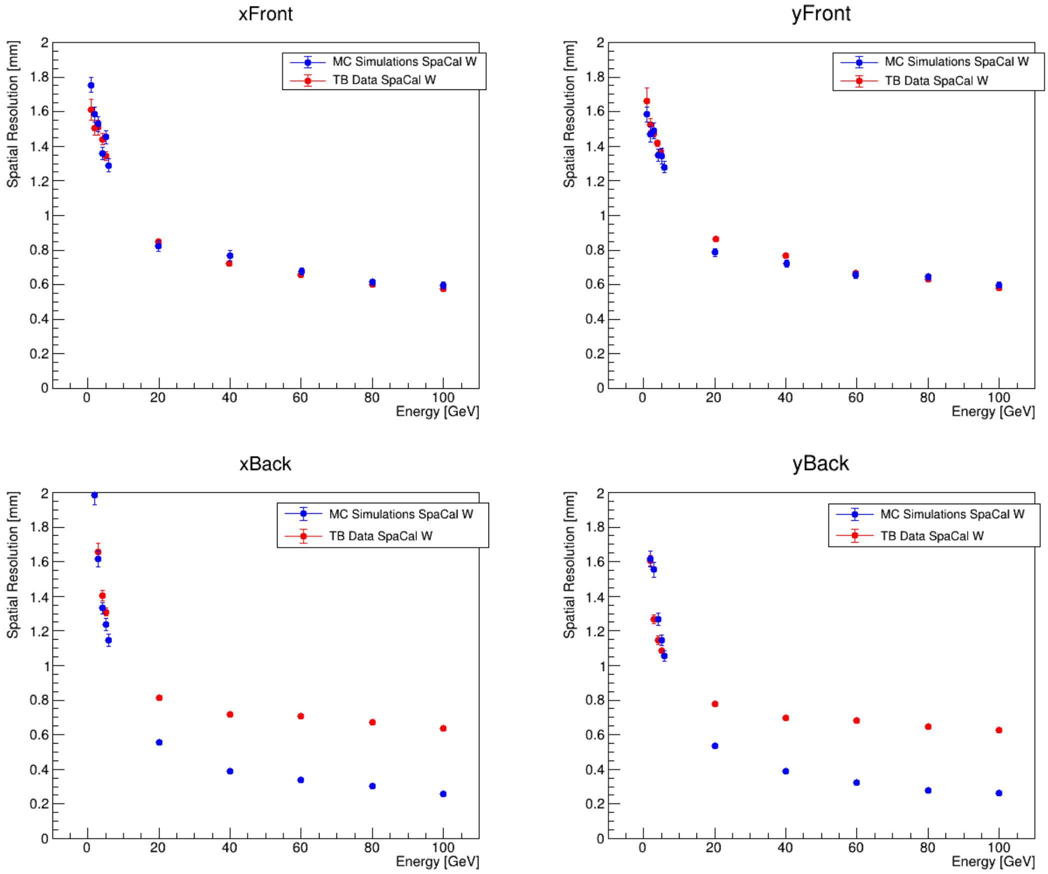

Figure 5.19: Spatial resolution obtained from the TB Data (red) and MC simulations (blue) as a function of the beam energy considering front and back sections separately for the SpaCal W rotated of 3° along the azimuthal and the altitude direction.

Moreover, it is possible to consider the overall position resolution along x and y by considering the two sections combined with the weighted mean method.

From the comparison shown in Figure 5.21 for the SpaCal W and in Figure 5.22 for the

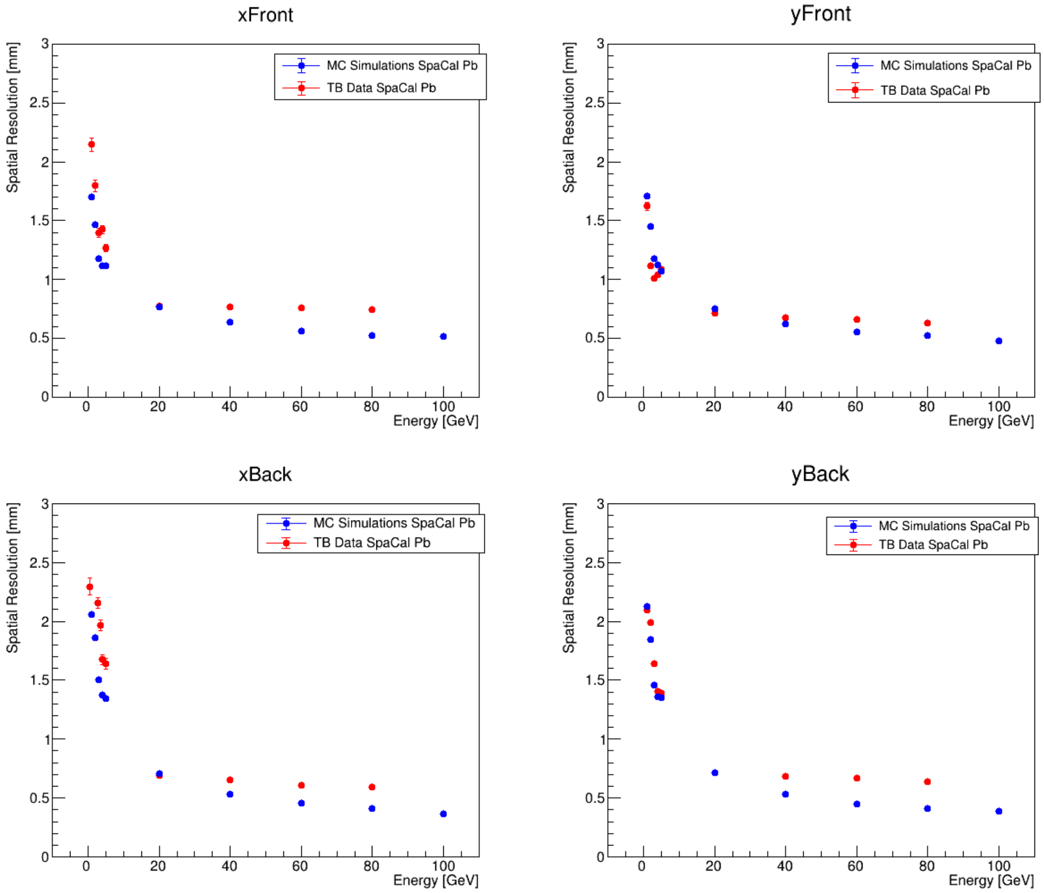

Figure 5.20: Spatial resolution obtained from the TB Data (red) and MC simulations (blue) as a function of the beam energy considering front and back sections separately for the SpaCal Pb rotated of 3° along the azimuthal and the altitude direction.

SpaCal Pb, it follows that the spatial resolution describes the same decreasing trend as the beam energy increases for both MC simulations and test-beam data. However, the non-perfect match between the two datasets still exists above 20 GeV.

The discrepancy between the measurements and the predictions could be associated with several effects.

For instance, the results are affected by the intrinsic position resolution of the DWCs, which is of the order of hundreds of μs. Besides this, one should take into account also the possibility that the energy measurements are worse in the test-beam data than in the MC simulations, as shown in Figure 2.10. This could be related to different contributions. For instance the noise term enters only in the energy resolution in the test-beam data analysis, as well as the energy calibration procedure, that is not needed for MC simulations since the response of the cells are all equal except for a front-back factor. An additional contribution comes from the non-ideality of the beam energy and

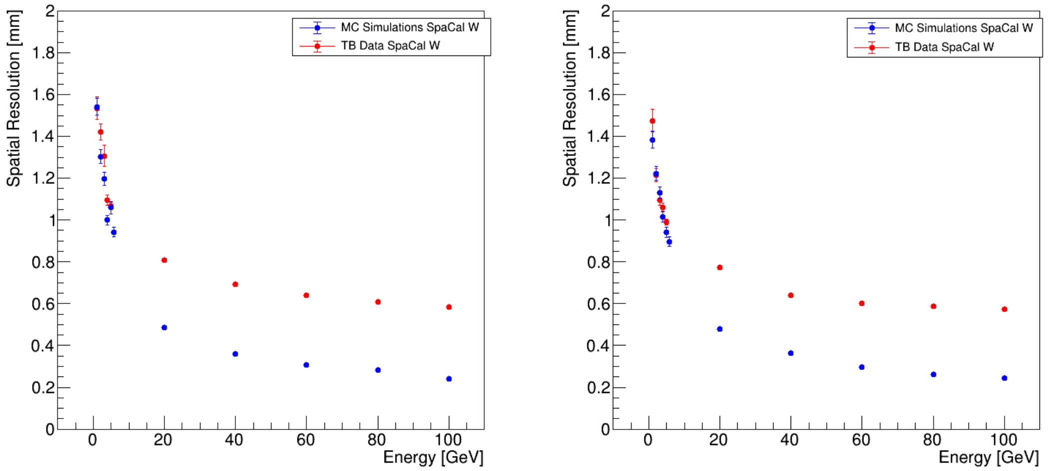

Figure 5.21: Spatial resolution along x (left) and y (right) from the TB Data (red) and MC simulations (blue) as a function of the beam energy considering front and back sections combined with the weighted mean method, for the SpaCal W rotated of 3° along the azimuthal and the altitude direction.

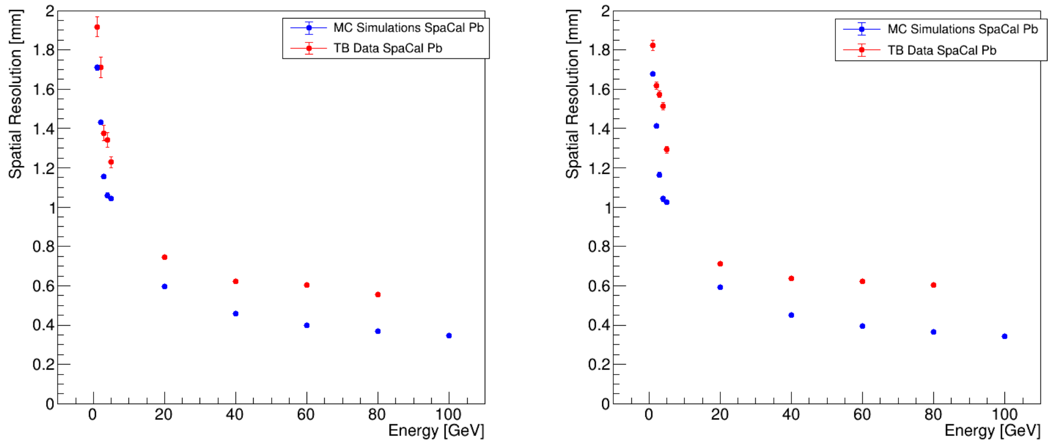

Figure 5.22: Spatial resolution along x (left) and y (right) from the TB Data (red) and MC simulations (blue) as a function of the beam energy considering front and back sections combined with the weighted mean method, for the SpaCal Pb rotated of 3° along the azimuthal and the altitude direction.

of the prototypes: crystals dimensions and purity can vary a little as well as the pitch between them inside the modules.
These factors, together with the beam impurities at SPS, were a source of systematic

uncertainties in the spatial resolution evaluation. Moreover, from the angular studies on the SpaCal W, it came out that there was an angular offset related to a non perfect alignment of the prototype with the beam. Since the spatial resolution has a dependency on the angle, and since the corrections applied are strongly related to the rotation of the module, the presence of an offset in the angle can lead to a worsening of the position results.

Lastly, a plot containing the results of experimental measurements and MC simulations for both SpaCal prototypes is shown in Figure 5.23.

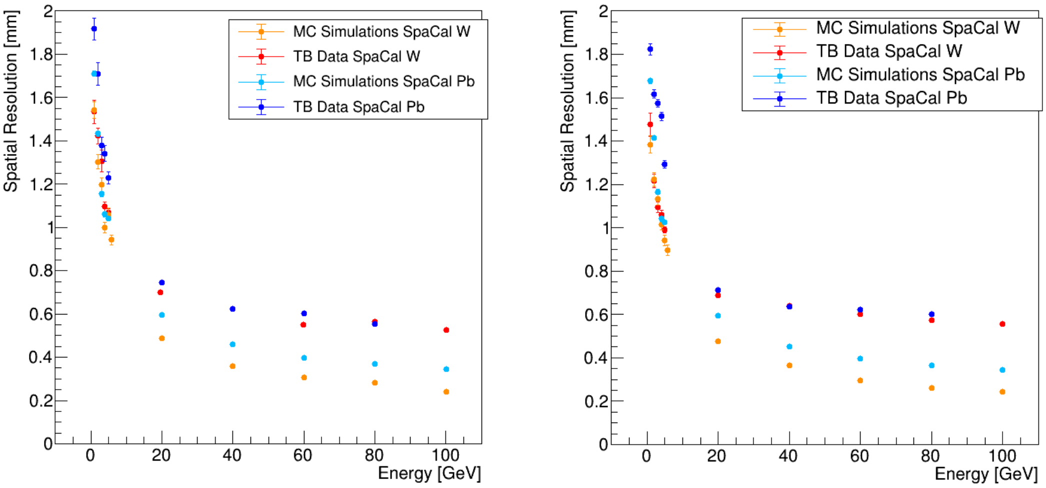

Figure 5.23: Spatial resolution along x (left) and y (right) from the TB Data and MC simulations as a function of the beam energy considering front and back sections combined with the weighted mean method, for the SpaCal Pb and the SpaCal W rotated of 3° along the azimuthal and the altitude direction.

Some general conclusions can be drawn from the summary graph that shows the spatial resolution values as a function of the beam energies tested at DESY and at SPS facilities.

Foremost, as already mentioned before, the performance of the SpaCal W in terms of position resolution are compatible with the ones of the SpaCal Pb. This behaviour is confirmed by both the test-beam results and the MC outcomes.

Secondly, the experimental measurements do not fit very well the simulations, particularly for energies above 20 GeV. Nonetheless, if one takes into account all the effects listed before it is possible to understand the reason for this discrepancy.

In conclusion, for energies higher than 20 GeV both the SpCal W and SpaCal Pb prototypes meet the requirements for the Upgrade II of the electromagnetic calorimeter, achieving an overall spatial resolution of less than 1 mm.

Chapter 6

Conclusions

Throughout this thesis, the performance of the most promising SpaCal prototypes designed for the Upgrade II of the LHCb electromagnetic calorimeter were discussed. As mentioned in the previous chapters, the modules involved in the future detector have to face a major challenge to operate at a higher radiation levels, with an increasing pile-up while trying to improve their efficiency. Achieving an angular resolution of the order of 1° and a position ability of the order of 1 mm for the central part of the future electromagnetic calorimeter is of fundamental importance to reach the goals set for the upgrade, such as the separation of overlapping electromagnetic showers, and to study theories with physics beyond the Standard Model that involve Long-Lived Particles.

After a technical overview of the new SpaCal technologies studied during this work, an initial introduction to the analysis is given in Chapter 3, followed by the general procedure applied to calculate spatial and angular resolution of the prototypes.
These topics were investigated in Chapter 4 with the "virtual" approach involving the use of a numerical simulator, essential to build a detailed Monte Carlo simulation program which reproduced accurately the test-beam setup, in order to better understand the experimental results.
Furthermore, the spatial and angular resolution were studied starting from the data acquired during various Beam Tests that took place at SPS and DESY facilities, where the SpaCal prototypes were tested in different configurations with an electron/positron beam in the energy range between 1 GeV and 100 GeV.

From the analysis of the test-beam measurements, the study of the outcome of the Monte Carlo simulations and the comparison between the two, it was possible to draw some general conclusions related to the SpaCal performance. The values obtained for the spatial and the angular resolution from the Beam Tests, that have also been confirmed by MC simulation results, demonstrated the potential of the GAGG fibres, not only in terms of radiation hardness but also for their position ability and angular resolution. On the other hand, the performances of the SpaCal Pb prototype are slightly worse than the SpaCal W, reaching values around 1 mm and >1° respectively for an high-energy beam. Nevertheless, the values obtained meet the challenging requirements for the Upgrade forseen for the LHC Phase II, being within the limits designed for the project for the innermost part of the calorimeter. The current performance of the SpaCal prototypes in fact allows an energy resolution sampling and constant terms of about 10 and 1% to be achieved, a position resolution that guarantees the separation of the overlapping showers, and a time performance that allows an accurate reconstruction of π_0 events as well as a reduction of the γ combinatorial background.

Given the excellent results for the SpaCal W prototype, future research projects will involve a further optimisation of the time performance of the GAGG crystals employed for the active part of the detector. Moreover the introduction of a timing layer in the new design would be of benefit to improve its time resolution up to 10 ps, pushing the electromagnetic calorimeter performance beyond its current limits.

References

[1] A. Augusto Alves, Jr. et al. *The LHCb Detector at the LHC.* JINST, 3:S08005, 2008.

[2] Lyndon Evans and Philip Bryant. *LHC Machine.* JINST, 3:S08001, 2008.

[3] LHCb collaboration, *Physics case for an LHCb Upgrade II. Opportunities in flavour physics, and beyond, in the HL-LHC era*, CERN-LHCC-2018-027.

[4] LHCb Collaboration, *Expression of Interest for a Phase-II LHCb Upgrade Opportunities in flavour physics, and beyond, in the HL-LHC era*, CERN-LHCC-2017-003 February 8, 2017.

[5] J. Albrecht, M. Charles, L. Dufour, M. Needham, C. Parkes, G. Passaleva, A. Schopper, E. Thomas, V. Vagnoni, M. Williams, G. Wilkinson, *Luminosity scenarios for LHCb Upgrade II*, LHCb-PUB-2019-001 February 28, 2019

[6] LHCb collaboration, *Framework TDR for the LHCb Upgrade II. Opportunities in flavour physics, and beyond, in the HL-LHC era*, CERN-LHCC-2021-012.

[7] Glenne F. Knoll *Radiation Detection and Measurements*, John Wiley & Sons, Third edition.

[8] R. Wigmans, *Calorimetry, Energy Measurements in Particle Physics* Internal series of Monograph on Physics, 2000.

[9] LHCb collaboration, *Photon and Neutral Pion reconstruction* LHCB 2003-091.

[10] CERN Yellow Reports, *High-Luminosity Large Hadron Collider (HL-LHC)Technical design report*, CERN-2020-010.

[11] Yuri Guz, *The Phase 2 Upgrade of the LHCb Calorimeter* 2020 JINST 15 C09046.

[12] M. Pizzichemi *The Phase II upgrade of the LHCb calorimeter system*, 2020 JINST 15 C05062.

[13] LHCb Calorimeter group, *Calibration and performance of the LHCb calorimeters in Run 1 and 2 at the LHC*, CERN-LHCb-DP-2020-001 August 26, 2020.

[14] L. Martinazzoli, LHCb SPACAL R&D group and Crystal Clear Collaboration *Crystal Fibers for the LHCb Calorimeter Upgrade*, IEEE TRANSACTIONS ON NUCLEAR SCIENCE, VOL. 67, NO. 6, JUNE 2020.

[15] L. Martinazzoli, N. Kratochwil, S. Gundacker, E. Auffray *Scintillation properties and timing performance of state-of-the-art* $Gd_3Al_2Ga_3O_{12}$ *single crystals*, Nuclear Inst. and Methods in Physics Research, A 1000 (2021) 165231.

[16] M.Pizzichemi, *Scintillating sampling ECAL technology for the Upgrade II of LHCb*, VCI 2022.

[17] L. An, E. Auffray, F. Betti, F. Dall'Omo, D. Gascon, A. Golutvin, Y. Guz, S. Kholodenko, L. Martinazzoli, J. Mazorra De Cos, E. Picatoste, M. Pizzichemi, P. Roloff, M. Salomoni, D. Sanchez, A. Schopper, A. Semennikov, P. Shatalov, E. Shmanin, D. Strekalina, Y. Zhang, *Performance of a spaghetti calorimeter prototype with tungsten absorber and garnet crystal fibres*, arXiv:2205.02500 [physics.ins-det]

[18] Physics Beyond Colliders collaboration, *SPS Beam Dump Facility*, arXiv:1912.06356; CERN-PBC-REPORT-2019-005; CERN-2020-002

[19] Elena Dall'Occo, *Searches for long-lived particles with LHCb*, Sixth Annual Conference on Large Hadron Collider Physics (LHCP2018), 4-9 June 2018